NASA TECHNICAL NOTE

NASA TN D-6683

RESULTS OF THE MARINER 6 AND 7 MARS OCCULTATION EXPERIMENTS

by Joseph S. Hogan, Richard W. Stewart, S. I. Rasool, and L. H. Russell

Goddard Space Flight Center
Greenbelt, Md. 20771

NATIONAL AERONAUTICS AND SPACE ADMINISTRATION • WASHINGTON, D. C. • MARCH 1972

1. Report No.	2. Government Accession No.	3. Recipient's Catalog No.
NASA TN D-6683		

4. Title and Subtitle
Results of the Mariner 6 and 7 Mars Occultation Experiments

5. Report Date
March 1972

6. Performing Organization Code

7. Author(s) Joseph S. Hogan, Richard W. Stewart, S. I. Rasool, and L. H. Russell

8. Performing Organization Report No.
G-1050

9. Performing Organization Name and Address
Goddard Space Flight Center
Greenbelt, Maryland 20771

10. Work Unit No.

11. Contract or Grant No.

12. Sponsoring Agency Name and Address
National Aeronautics and Space Administration
Washington, D.C. 20546

13. Type of Report and Period Covered
Technical Note

14. Sponsoring Agency Code

15. Supplementary Notes

16. Abstract

An analysis of the Mariner 6 and 7 occultation data has been completed. Final profiles of temperature, pressure, and electron density on Mars have been obtained for the Mariner 6 and 7 entry and exit cases, and results are presented for both the lower atmosphere and ionosphere. The results of a detailed analysis of the systematic and formal errors introduced at each stage of the data-reduction process are also included.

At all four occultation points, the lapse rate of temperature was subadiabatic up to altitudes in excess of 20 km. A pronounced temperature inversion was present above the surface at the Mariner 6 exit point. All four profiles exhibit a sharp, superadiabatic drop in temperature at high altitudes, with temperatures falling below the frost point of CO_2. These results give a strong indication of frozen CO_2 in the middle atmosphere of Mars.

The analysis for the upper atmosphere indicates peak electron populations of $(1.59 \pm 0.2) \times 10^5$ cm^{-3} near 136.5 km and $(1.73 \pm 0.2) \times 10^5$ cm^{-3} near 137.5 km at Mariner 6 and 7 entry points, respectively. The plasma scale heights above these maxima were 43 ± 6 km and 47 ± 4 km, corresponding to topside temperatures of 388 ± 54 K and 424 ± 35 K for Mariner 6 and 7 entries, respectively.

17. Key Words (Selected by Author(s))	18. Distribution Statement
Mariners 6 and 7 Occultation Experiment Martian Atmosphere Mars Ionosphere	Unclassified—Unlimited

19. Security Classif. (of this report)	20. Security Classif. (of this page)	21. No. of Pages	22. Price
Unclassified	Unclassified	37	$3.00

*For sale by the National Technical Information Service, Springfield, Virginia 22151

CONTENTS

RESULTS OF THE MARINER 6 AND 7 MARS OCCULTATION EXPERIMENTS

by

Joseph S. Hogan
Richard W. Stewart
S. I. Rasool
Goddard Space Flight Center

and

L. H. Russell
Computer Sciences Corporation

INTRODUCTION

The Mariner 4 S-band occultation experiment (Kliore et al., 1965) and ground-based spectroscopic observations (Owen, 1966; Spinrad et al., 1966; Belton and Hunten, 1966) established that the pressure at the surface of Mars is typically less than 10 mb and that CO_2 is the major constituent of the atmosphere. From its thinness and composition, one can conclude that the Martian atmosphere approaches radiative equilibrium at low altitudes, with diurnal temperature adjustments near the surface (Gierasch and Goody, 1968). The results of the preliminary analysis of the Mariner 6 and 7 occultation data for the lower atmosphere (Kliore et al., 1969) were largely inconsistent with this conclusion, however, with several features of the derived temperature profiles differing surprisingly from theoretical predictions. These results seemed to indicate that important and hitherto unsuspected physical processes might be at work in the lower atmosphere of Mars. For example, at the Mariner 6 entry point, an unexpectedly warm, nearly isothermal layer underlying a region of precipitously falling temperature was found in the middle atmosphere. Neither of these features had ever been produced in any thermal model, and to account for their presence, considerable modification of the widely accepted radiative-convective theory of the lower Martian atmosphere would be required.

In an attempt to resolve this discrepancy between theory and observation, which has an important bearing on our understanding of the meteorology of Mars, an independent analysis of the Mariner 6 and 7 occultation data has been performed at Goddard Space Flight Center's Institute for Space Studies (GISS). A reanalysis of the data was also conducted at the Jet Propulsion Laboratory (JPL) by the experimental team, with results described by Kliore et al. (1970).

The GISS investigation has involved the construction of two separate computer programs for—

(1) Combining Doppler residual data with trajectory data to obtain the raw residuals as a function of the distance of the Mariner spacecraft from the limb of Mars.

(2) Filtering from the raw residual data those components not due to the Martian atmosphere.

(3) Integrating the filtered residuals over time to derive the phase change as a function of the spacecraft's distance from the planetary limb.

(4) Inverting the phase-change data, with a suitable correction for refractive bending, to obtain profiles of refractivity in the Martian atmosphere.

(5) Deriving temperature, pressure, and electron-density profiles on Mars from the refractivity distributions.

(6) Computing the systematic and formal errors introduced at each of the above stages of the analysis.

Earlier (Rasool et al., 1970), the authors described their partial and preliminary results concerning the temperature distributions in the lower Martian atmosphere at the four occultation points. Those results differed in several important respects from the preliminary findings of Kliore et al. (1969). For example, the warm, nearly isothermal region in the middle atmosphere found in the Mariner 6 entry temperature profile of Kliore et al. (1969) was not present in the corresponding profile of Rasool et al. (1970). However, agreement with Kliore et al. (1969) was obtained with regard to the suggestion of extremely low temperatures at higher altitudes on Mars. Also, the results of Rasool et al. (1970) were in general agreement with the set of corrected thermal profiles presented by Kliore et al. (1970). Discrepancies between the first results of Kliore et al. (1969) and the later findings of the JPL and GISS groups were attributed to unsatisfactory correction of the Doppler data in the preliminary analysis.

The authors have now obtained final profiles of temperature, pressure, and electron density on Mars from the occultation data for the Mariner 6 and 7 entry and exit cases, and the results are presented for both the lower atmosphere and the ionosphere of Mars. Also included are the results of a detailed analysis of the systematic and formal errors introduced at each stage of the data-reduction process.

GENERAL PRINCIPLES AND REQUIRED ASSUMPTIONS

The possibility of determining certain properties of a planetary atmosphere by monitoring the telemetry link between the Earth and a space probe on an occulting trajectory was first discussed by Fjeldbo and Eshleman (1965). As the probe approaches the limb of the planet, the phase path, frequency, and amplitude of the signal are altered by its passage through the planetary atmosphere. The local index of refraction differs from unity in the neutral atmosphere and ionosphere, which causes the phase and group velocities to depart from their free-space values. As the mean refractive index along the ray path varies with the distance of the path from the limb of the planet, differential bending of the rays occurs, producing focusing and defocusing of the signal.

The changes in the signal characteristics are a function of the distribution of the index of refraction in the atmosphere of the planet. In principle, if these changes are recorded as the spacecraft passes behind the planet, the distribution of refractive index can be inferred.

The present investigation is concerned with the determination of atmospheric parameters on Mars from the Mariner 6 and 7 phase-change data. The phase changes produced by the Martian atmosphere must be obtained by subtracting all predictable phase shifts due to light transit time, spacecraft motion, Earth rotation, and so forth from the total phase change during the period of the experiment. Since the effect of the atmosphere is small in comparison with these other effects, high accuracy is required at this stage in the data-reduction process; of prime importance is a precise knowledge of the spacecraft trajectory and range rate. If the necessary accuracy is achieved, model fitting or, alternately, integral inversion of the residual phase changes can be used to estimate the properties of the atmosphere.

The residual phase change is in general a result of the combined effects of the neutral atmosphere and ionosphere of the planet. Since the contribution of the neutral atmosphere to the phase change is proportional to the total atmospheric density along the ray path, this component will be largest when the ray path is close to the limb of the planet. On the other hand, the effects of the ionosphere on the phase change are proportional to the integrated ion content along the ray path, and these effects will be greatest when the ray path lies at a distance from the limb approximately equal to the height of the ionosphere above the surface. If the neutral and ionized regions which produce a detectable change in the signal characteristics are separated in altitude, it should be possible to obtain information on both regions from a single-frequency experiment.

Obviously, the measured variation of residual phase change with distance from the planetary limb does not uniquely determine the spatial distribution of refractive index in the atmosphere; consequently, some *a priori* assumptions must be made in interpreting the atmospheric phase-change data. The assumption of a spherically symmetric, stratified atmosphere simplifies model fitting and permits the use of integral inversion techniques in deriving a refractivity distribution from the observed phase changes. Since a highly localized region of the lower atmosphere is probed by the telemetry signal, the assumption of spherical symmetry is equivalent, in this case, to postulating that vertical gradients of refractivity in the lower atmosphere are much larger than horizontal gradients—an assumption often used in atmospheric physics. The assumption of spherical symmetry in the Martian ionosphere is difficult to justify, however, and the effects of possible departures from this condition in the region probed on the interpretation of the phase data should be considered. For example, in the ionosphere, the electron densities are likely to be symmetric about the subsolar point; thus, the degree to which the nonspherical nature of the ionosphere affects the interpretation of the phase data should depend on the local zenith angle at the point of occultation.

From the above discussion, it should be clear that only if the following three conditions are met can the single-frequency occultation experiment succeed in providing accurate information on the distributions of temperature, neutral density, and electron concentration in the Martian atmosphere: (1) The changes in the telemetry signal that result from the Martian atmosphere can be isolated from the changes that result from all other effects; (2) a physical separation in altitude exists between the neutral and ionized regions which produce these changes; and (3) the distribution of refractivity in

the atmosphere must not contradict a basic assumption about the atmospheric structure, that horizontal gradients of refractivity are much smaller than vertical gradients.

CORRECTION OF DOPPLER RESIDUAL INPUT DATA

The present analysis is based upon the Mariner 6 and 7 closed-loop Doppler residual and trajectory data supplied by the JPL experimental team. During the near encounter of Mariner 6 with Mars at 0519 GMT, July 31, 1969, Deep Space Network (DSN) Stations 12 and 14 at Goldstone, California, monitored the spacecraft telemetry. At the time of the closest approach of Mariner 7 (0501 GMT on August 5, 1969), Station 41 at Woomera, Australia, was also in position to communicate with that spacecraft, and all three stations monitored the telemetry in this case. Ten distinct sets of Doppler residual data are available, including two each (Stations 12 and 14) for Mariner 6 occultation entry and exit, and three each (Stations 12, 14, and 41) for Mariner 7 occultation entry and exit.

Four additional bodies of data with slightly reduced noise levels can be obtained by averaging the data from the different stations in operation during the Mariner 6 and 7 encounters. This averaging procedure reduces the level of the noise that originates independently at each receiving station during the experiment, such as the effects of changes, due to turbulence, in the refractivity along the ray path through the Earth's atmosphere. Averaging over stations does not remove or reduce the component of the noise produced by the spacecraft systems, which must be identical at all stations.

Entry data were taken in a two-way mode, with a frequency generated by a rubidium standard transmitted to the spacecraft, which coherently retransmitted it to Earth. Exit data were acquired in a one-way mode, with a crystal oscillator onboard the spacecraft providing the reference signal for transmission to Earth. As a consequence of the two different modes of operation, immersion data reflect a two-way passage through the atmosphere of Mars, whereas emersion data reflect a one-way passage. Also, according to Fjeldbo et al. (1970), the stability of the rubidium standard used in acquiring the entry data (a few parts in 10^{12}) is greater by nearly two orders of magnitude than the stability of the onboard crystal oscillators used during exits (about one part in 10^{10}).

Both the Doppler residual data points and the trajectory points have been supplied at 1-s time intervals. However, the trajectory data are shifted in time from the residual data by a fraction of a second; thus, the position of the spacecraft at the times at which the residual points are given must be obtained by interpolation. This interpolation was performed in the present analysis through the use of a third-order-polynomial spline fit to the trajectory data.

Also, in each case, it was necessary to extrapolate the Doppler residual data to obtain the value of the residual at the precise time of occultation entry or exit. Since both spacecraft approached occultation with velocities close to 3 km/s perpendicular to the Earth-Mars line, a careful extrapolation of the residuals is of the utmost importance for an accurate determination of the atmospheric conditions at the surface of Mars. Because the refractivity decreases exponentially with altitude above the surface of the planet, it can be anticipated that a rapid variation of the residuals will occur immediately prior to and after occultation. To obtain a value for the Doppler residual at the moment of occultation, the 10 residual points preceding or following occultation were least-squares fitted with a third-order polynomial. This polynomial was extrapolated (over an interval of less than 1 s) to the occultation time to obtain the residual value at the instant of occultation.

The input Doppler residual data are characterized by large quasi-linear drifts during the periods before and after occultation of the spacecraft by Mars. Almost identical patterns are found in the two or three different sets of data corresponding to a single entry or exit point. As an example, Figures 1 through 4 show the raw Doppler residual data from Station 12 for the four occultation points on Mars. Except for minute differences due to random noise (which can presumably be eliminated by the averaging described above), the data from the other stations are indistinguishable to the eye from the Station 12 data shown in these figures.

The trends evident in the input data of Figures 1 through 4 are probably due to the combined effects of oscillator drifts and trajectory errors.* Because they extend far into preencounter and post-encounter periods, it is clear that they are in no way related to the atmospheric characteristics on Mars. However, it is not possible to point to the exact cause of these drifts in the residual data; thus, their functional form cannot be specified with certainty.

To determine the properties of the Martian atmosphere from the residual data, the unwanted effects evident in Figures 1 through 4 were removed by subtraction of least-squares-fitted bias curves. In our preliminary analysis, a fitted curve of the form $A + Bt + C \sin t + D \cos t$ was subtracted from the data (Rasool et al., 1970). Two additional avenues of approach have been used in the present study. In one test, Fourier series of varying complexity were fitted to the data in the preencounter and post-encounter periods; in another, polynomials of different orders were fitted to the preencounter and postencounter data.

For both Mariners 6 and 7, preencounter and postencounter periods were defined as the periods ending 130 s before occultation entry and beginning 40 s after occultation exit, respectively. With these definitions, the preencounter and postencounter periods end and begin, respectively, when the ray path is about 360 km from the limb of Mars along the perpendicular to the Earth-Mars line.

Seven-term Fourier series and third-order polynomials can be fitted to all of the preencounter or postencounter Doppler-data sets with standard deviations of less than 0.1 Hz. This same degree of fit was found in the analysis reported earlier (Rasool et al., 1970). Although series with as many as 19 terms and polynomials of as many as nine orders were considered in these experiments, no significant improvement of the fits to the preencounter and postencounter data was realized by considering series with more than seven terms or polynomials of order higher than third. The use of 19-term Fourier series and ninth-order polynomials produces a decrease of less than 0.02 Hz in the above standard deviations.

Interestingly, the relative stability of the entry and exit frequency references described by Fjeldbo et al. (1970) is not reflected in the noise level of the data about the fitted curves.

Unfortunately, difficulties arise when an attempt is made to extrapolate the higher-order fitted curves from the preencounter and postencounter periods into the regions where the atmospheric effects are present. In the case of the more complex functions considered, the addition of a single point to the group of data fitted can produce drastic changes in the extrapolated portion of the curve. This sensitivity is due to improper functional representation of the mechanisms that produce the drifts in the raw residual data. It is not difficult to imagine that the improper selection of one of these

*Kliore, private communication.

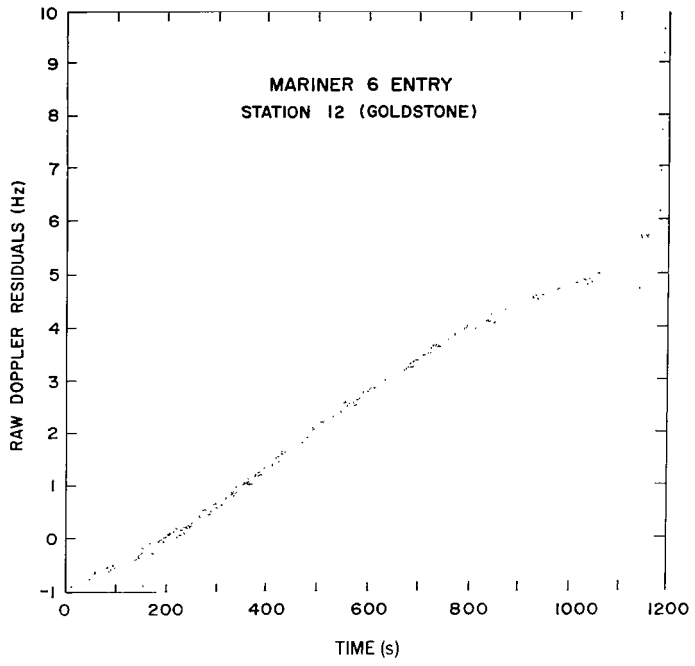

Figure 1—Raw Doppler residual data (Station 12) for Mariner 6 entry case. The abscissa is an arbitrary time scale.

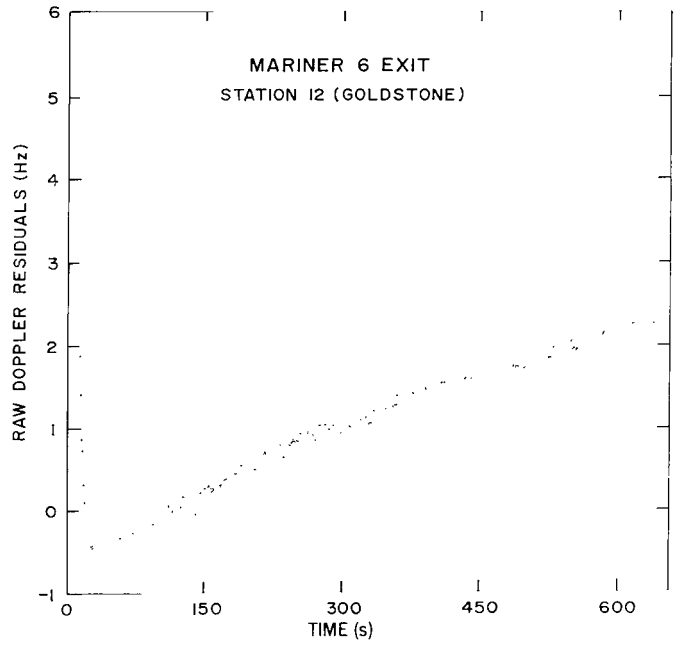

Figure 2—Raw Doppler residual data (Station 12) for Mariner 6 exit case. The abscissa is an arbitrary time scale.

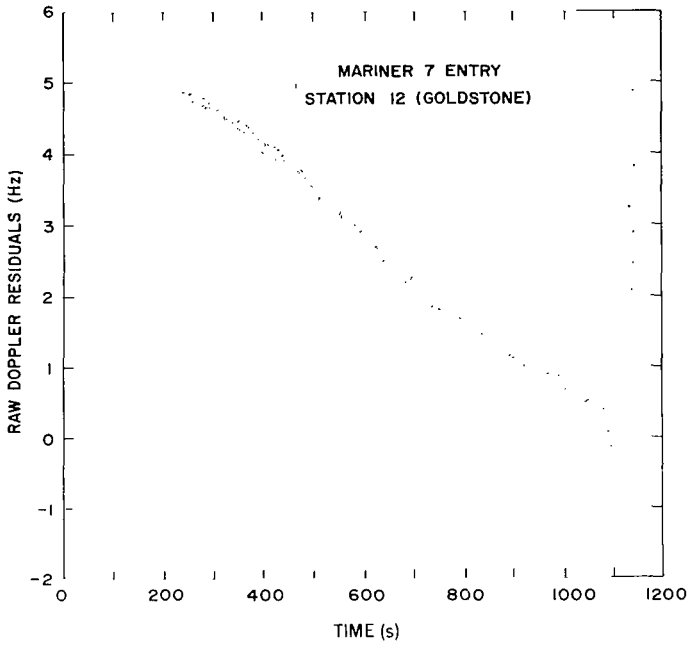

Figure 3—Raw Doppler residual data (Station 12) for Mariner 7 entry case. The abscissa is an arbitrary time scale.

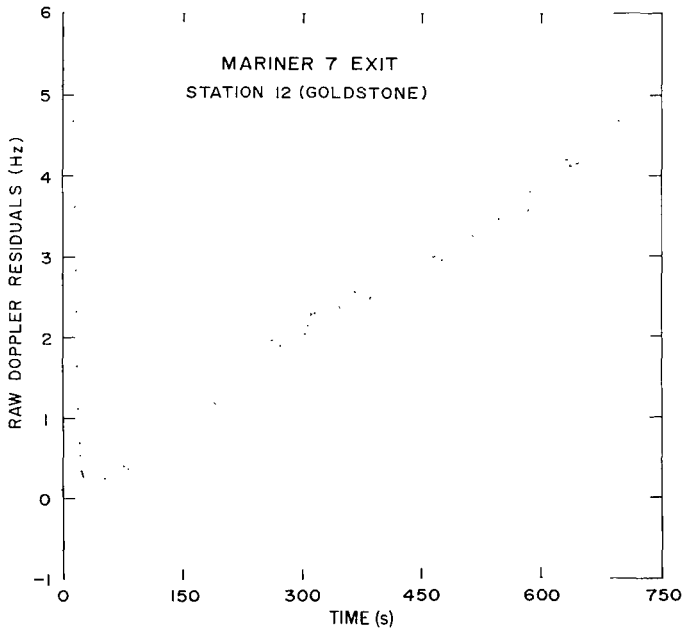

Figure 4—Raw Doppler residual data (Station 12) for Mariner 7 exit case. The abscissa is an arbitrary time scale.

curves would result in a complete misrepresentation of the component of the raw Doppler data that is due to the Martian atmosphere.

Changes in the extrapolated portions of the fitted functions as the sample of points fitted is varied are significantly smaller when simpler functions are considered. Nevertheless, on the basis of the somewhat inconsistent behavior exhibited by even the simpler of the fitted functions, the problem of objectively removing the drifts from the raw residual data without having precise information on the mechanisms that gave rise to these drifts would seem hopeless.

To ensure the extraction of significant information on the Martian atmosphere from these bodies of data, it is necessary to apply an additional constraint on the acceptability of the fitted curves, beyond that of a small standard deviation in the preencounter or postencounter period. Such a criterion is suggested by one of the basic assumptions required for the success of the occultation experiment—that somewhere in the middle atmosphere of Mars, a region of essentially zero (undetectable) refractivity exists. Unless this assumption is valid, the effects of the ionosphere and neutral atmosphere on Mars cannot be unambiguously separated.

With this assumption, a curve that properly represents the nonatmospheric component in the raw residual data must be (1) one that can be fitted with a small standard deviation to the data in the preencounter or postencounter region and (2) one whose removal from the raw residual data will eventually produce a profile of refractivity on Mars, characterized by an undetectably low refractivity value over an extensive region of the middle atmosphere. This desirable feature of a refractivity profile will henceforth be referred to as a *zero-refractivity ledge.* (In this experiment, an undetectably low value of refractivity corresponds to an absolute value less than 0.05 n-unit). To derive curves with both of the above characteristics, the following procedure was followed.

Polynomials of various orders were fitted to a particular group of preencounter or postencounter raw Doppler residuals. Each curve fitted was subsequently extrapolated into the region immediately prior to or after occultation where atmospheric effects are manifest and subtracted from the entire body of raw data to obtain a set of corrected residuals. These corrected residuals were then processed (as described below) to derive a distribution of refractivity as a function of the distance from the center of the planet to the point of closest approach of a ray. The refractivity profile was then examined for consistency with the assumption of a zero-refractivity ledge. The ledge value for each case was determined by scanning for the minimum of the absolute value of the refractivity in the middle atmosphere.

If consistency with the zero-ledge assumption for the Martian mesosphere was not found (refractivity ledge of absolute value greater than 0.05 n-unit), the fitted curve was rejected as an unacceptable representation of the nonatmospheric component of the raw residuals in the extrapolated region. If consistency was obtained (refractivity ledge of absolute value less than 0.05 n-unit), the refractivity distribution was used to derive distributions of temperature, pressure, and electron density for a chosen atmospheric composition. The entire procedure was then repeated, with another point being added to the group of preencounter or postencounter raw residuals to be fitted.

A similar sequence of operations was used to select acceptable Fourier representations of the nonatmospheric component of the Doppler residual input data.

It should be noted that for all 10 individual sets of raw data and for all four sets of averaged data, several hundred different bias curves consistent with the zero-ledge assumption could be closely fitted to preencounter or postencounter data groups. All of the alternatives in each case produced closely similar results (described below) when the analysis was carried through to obtain profiles of temperature, pressure, and electron density.

Typical sets of residual data for the four points of occultation on Mars, corrected via the method outlined above, are shown in Figures 5 through 8. These correspond to averages over the stations that monitored the telemetry at each point, and they closely resemble the mean of the several hundred sets of corrected residual data that were found to produce refractivity profiles satisfying the zero-ledge criterion.

DATA REDUCTION

The basic geometry of the occultation experiment is illustrated in Figure 9. Fjeldbo and Eshleman (1968) have shown that this simple geometry approximates to a high degree of accuracy the actual occultation configuration for a thin atmosphere. At the time of entry into and exit from occultation, the Mariner 6 spacecraft was approximately 9700 km and 17 700 km behind Mars, respectively. In the case of Mariner 7, the distances behind the planet were 8500 km at immersion and 19 800 km at emersion. The Earth-Mars distances were about 95.7 million km and 100.2 million km, respectively, at the times of the Mariner 6 and 7 encounters.

The analysis begins with a set of N Doppler residuals δ_i, corrected by the procedure detailed above, and a set of N spacecraft coordinates X_{s_i}, Z_{s_i}, corresponding to N points of time t_i. The index i increases and decreases with time in the cases of entry and exit, respectively; thus, point 1 corresponds to the farthest distance from the planet, the point at which the analysis is begun, and point N corresponds to the surface of the planet. With reference to Figure 9, the altitude h_i is given by

$$h_i = X_i - X_p \ , \tag{1}$$

where X_i is the distance from the center of Mars of the point of closest approach of a ray corresponding to the X_{s_i}, Z_{s_i} position of the spacecraft, and X_p is the planetary radius at the occulation point.

The phase change ϕ_i corresponding to the altitude of closest approach h_i at time t_i is obtained by time integration of the Doppler residuals according to the trapezoidal rule:

$$\phi_i = \left(\frac{\delta_1 + \delta_2}{2}\right) \Delta t_{1,2} + \left(\frac{\delta_2 + \delta_3}{2}\right) \Delta t_{2,3} + \cdots + \left(\frac{\delta_{i-1} + \delta_i}{2}\right) \Delta t_{i-1,i} \quad (\text{for } i > 1) \ , \tag{2}$$

where $\Delta t_{i-1,i}$ is the time interval between the Doppler residual measurements at times t_{i-1} and t_i. In the entry cases, integration was begun approximately 130 s before immersion, at the end of the preencounter period defined above, and carried forward in time. In the exit cases, the time order of the integration was reversed, with the integration starting at the beginning of the postencounter period, 40 s after emersion, and extending backward into the period where atmospheric effects are present.

In the bent-ray approximation of Figure 9, the distance of the closest approach of a ray from the center of the planet is related to the spacecraft coordinates and phase-path increase by

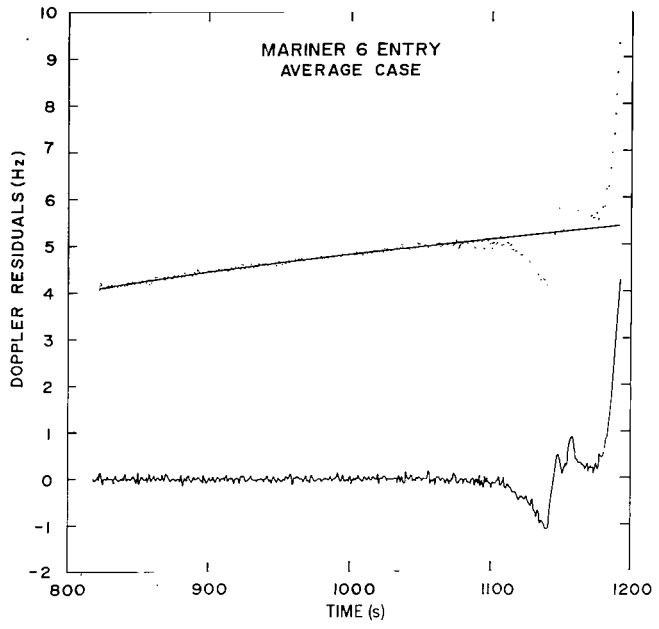

Figure 5—Raw Doppler residuals (dots), polynomial least-squares fit (smooth curve), and corrected residuals (noisy curve) corresponding to Mariner 6 entry. The residuals are averages of Station 12 and 14 data. The abscissa is an arbitrary time scale.

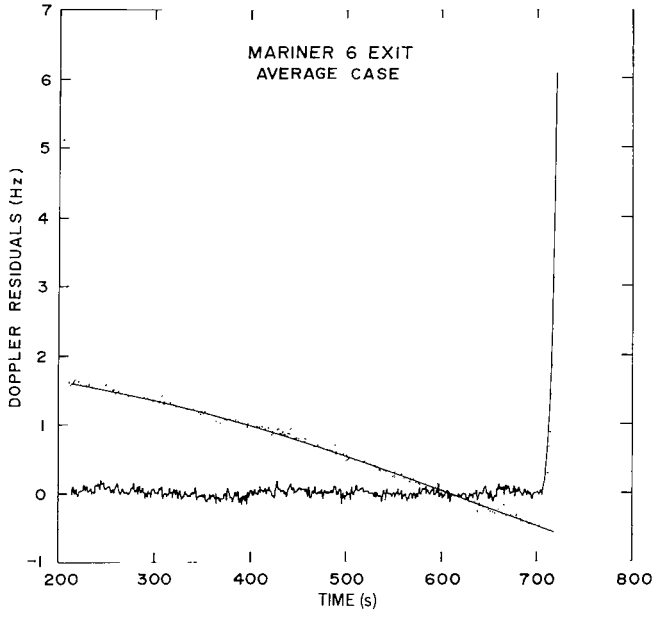

Figure 6—Raw Doppler residuals (dots), polynomial least-squares fit (smooth curve), and corrected residuals (noisy curve) corresponding to Mariner 6 exit. The residuals are averages of Station 12 and 14 data. The abscissa is an arbitrary time scale.

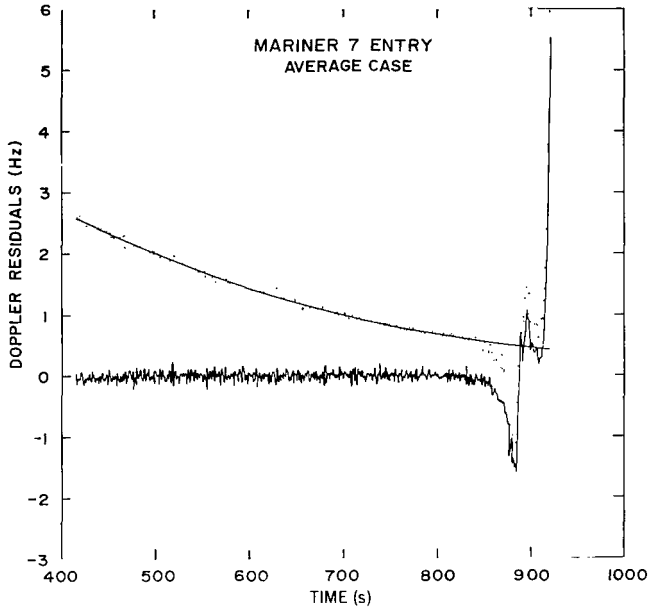

Figure 7—Raw Doppler residuals (dots), polynomial least-squares fit (smooth curve), and corrected residuals (noisy curve) corresponding to Mariner 7 entry. The residuals are averages of Station 12, 14, and 41 data. The abscissa is an arbitrary time scale.

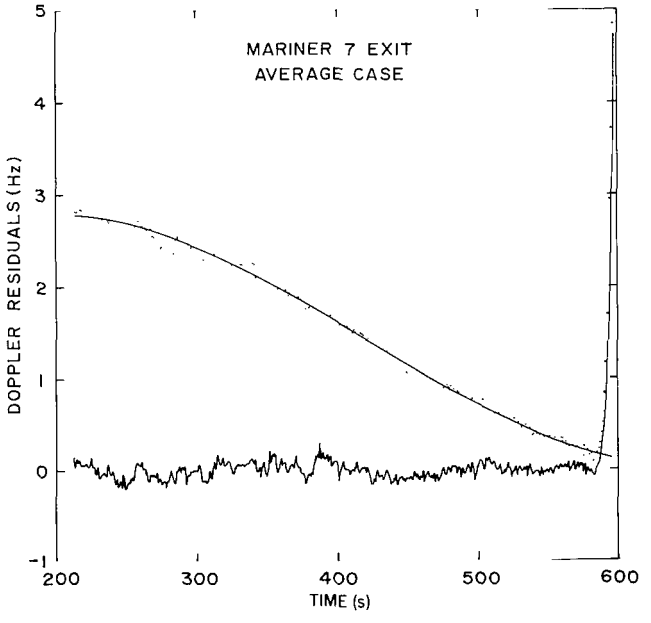

Figure 8—Raw Doppler residuals (dots), polynomial least-squares fit (smooth curve), and corrected residuals (noisy curve) corresponding to Mariner 7 exit. The residuals are averages of Station 12, 14, and 41 data. The abscissa is an arbitrary time scale.

$$X_i = X_{s_i} - Z_{s_i} \tan \alpha_i \ , \tag{3}$$

where α_i is the angle by which the path of the signal is bent from a straight line by the atmosphere:

$$\alpha_i = -\frac{\lambda \delta_i}{V_{s_i}} , \tag{4}$$

where V_{s_i} is the component of the spacecraft velocity along the perpendicular to the Earth-Mars line and λ is the wavelength of the telemetry signal (about 13.6 cm for both spacecraft).

The straight-line approximation to the phase change Φ is, with reference to Figure 9,

$$\Phi_i = \phi_i - \frac{Z_{s_i}}{\lambda \cos \alpha_i} + \frac{Z_{s_i}}{\lambda} \ . \tag{5}$$

For small α_i, expanding $\cos \alpha_i$ and neglecting higher-order terms causes Equation 5 to reduce to

$$\Phi_i = \phi_i - \frac{Z_{s_i} \alpha_i^2}{2\lambda} \ . \tag{6}$$

The straight-line portion of the total phase change is due to a region of nonzero refractivity, the Martian atmosphere, encountered along the path of the telemetry signal. The contribution to the total phase change represented by the second term on the right-hand side of Equation 6, is associated with the bending of the propagation path from a straight line.

The relationship of the straight-line phase change to the refractivity distribution in the atmosphere is given by

$$\Phi_i = \frac{10^{-6}}{\lambda} \int_{-\infty}^{+\infty} R(r)\, dZ \ , \tag{7}$$

where $R(r)$ represents the refractivity of an element of unit volume located on the ith ray path at a distance r from the center of the planet:

$$r^2 = X_i^2 + Z^2 \ . \tag{8}$$

Fjeldbo and Eshleman (1968) have outlined a numerical technique for obtaining the refractivity distribution in the case of a spherically symmetric Martian atmosphere, where $R(r)$ is a constant. The geometry applicable in this case is illustrated in Figure 10, adapted from their Figure 18. Under this assumption, N rays pass through an atmosphere consisting of N spherical layers, each of constant thickness and constant refractivity. The integral of Equation 7 may then be replaced by a linear equation of the form

$$\Phi_i = \frac{10^{-6}}{\lambda} \left(R_i \Delta Z_{i,i} + 2 \sum_{j=1}^{i-1} R_j \Delta Z_{i,j} \right) \ , \tag{9}$$

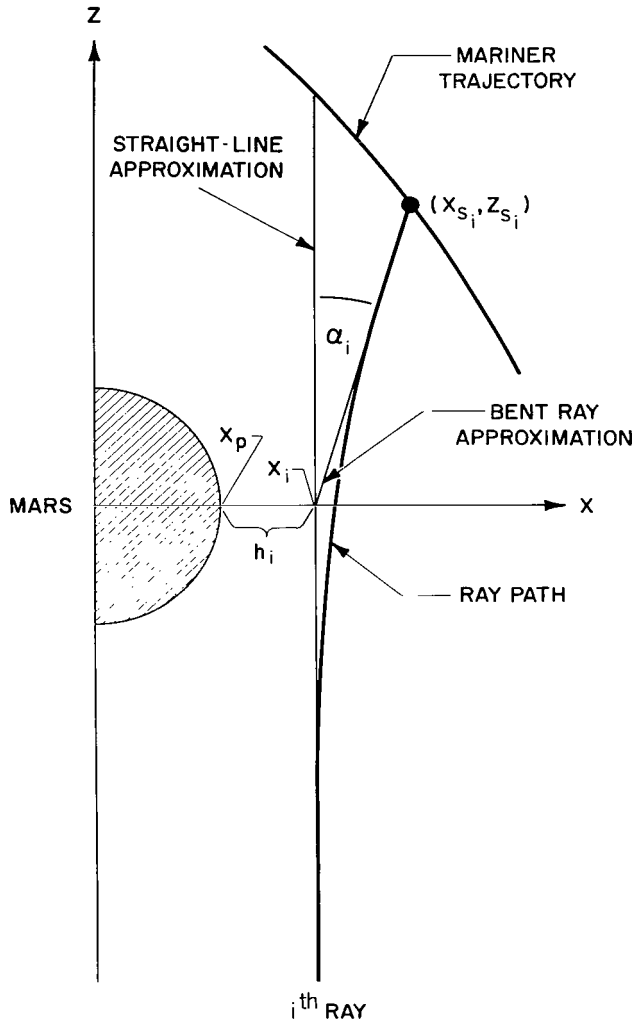

Figure 9—Ray path geometry (adapted from Fjeldbo and Eshleman, 1965).

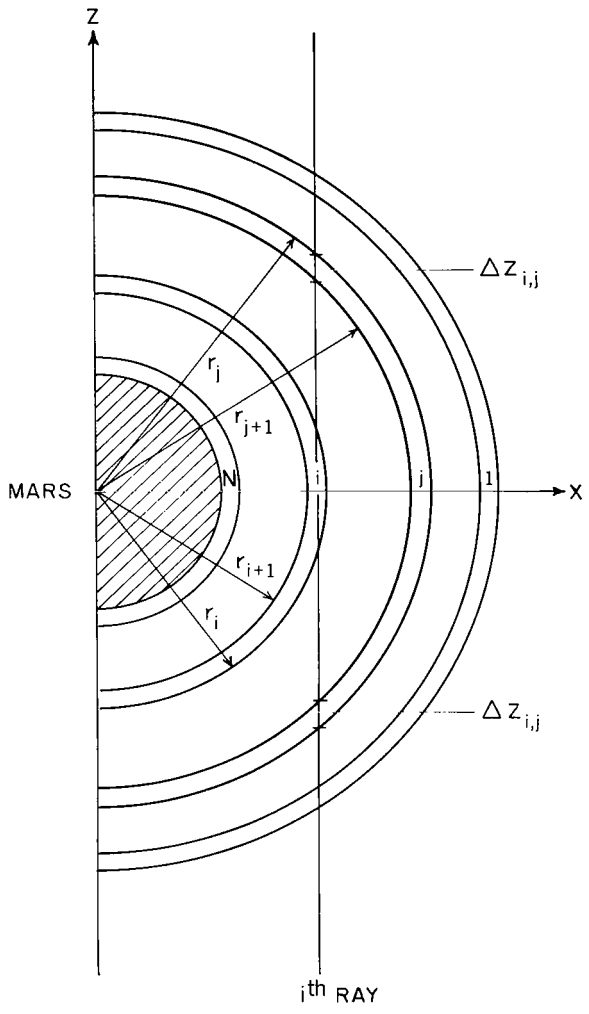

Figure 10—Geometry applicable to a spherically symmetric Martian atmosphere (adapted from Fjeldbo and Eshleman, 1968).

where R_j is the refractivity of the jth layer and $\Delta Z_{i,j}$ designates one-half the distance traversed by the ith ray in the jth layer. Referring to Figure 10, one sees that the relationship of $\Delta Z_{i,j}$ to the radii of the atmospheric layers is

$$\Delta Z_{i,j} = \left[r_j^2 - \left(\frac{r_i + r_{i+1}}{2} \right)^2 \right]^{1/2} - \left[r_{j+1}^2 - \left(\frac{r_i + r_{i+1}}{2} \right)^2 \right]^{1/2} \tag{10}$$

when i is greater than j, and

$$\Delta Z_{i,j} = 2\left[r_i^2 - \left(\frac{r_i + r_{i+1}}{2}\right)^2\right]^{1/2} \tag{11}$$

when $i = j$.

The set of N linear equations of the form of Equation 9 may be solved for R to yield the distribution of refractivity in the atmosphere of Mars:

$$R_1 = (\lambda \cdot 10^6 \Phi_1)/\Delta Z_{1,1}$$

and

$$R_i = \left(\lambda \cdot 10^6 \Phi_i - 2\sum_{j=1}^{i-1} R_j \Delta Z_{i,j}\right) \frac{1}{\Delta Z_{i,i}} \quad (\text{for } i \geq 2) . \tag{12}$$

To extract the distribution of neutral-particle number density in the lower atmosphere from this refractivity distribution, the chemical composition of the atmosphere must be specified. Ground-based infrared spectroscopic observations (Owen, 1966; Spinrad et al., 1966; Belton and Hunten, 1966) indicate that CO_2, with a partial pressure of 5 ± 2 mb, is the major constituent of the Martian atmosphere. Such measurements also show that the actual and possible abundances for other gases which possess infrared spectra are too low for these gases to contribute significantly to the atmospheric refractivity. However, gases inactive in the infrared, such as N_2, Ar, or Ne, could be present on Mars in significant amounts but would not be observable from the Earth's surface. For example, according to the results of the ultraviolet spectroscopy experiments on Mariners 6 and 7, as much as 5 percent of the Martian atmosphere could be N_2 (Barth et al., 1969; Dalgarno and McElroy, 1970).

It is assumed here that no gases other than CO_2, N_2, and Ne contribute to the observed refractivity on Mars. The molecular refractivities n for the nonpolar molecules CO_2 and N_2 are 1.84×10^{-17} and 1.10×10^{-17}, respectively, according to the data of Essen and Froome (1951). Tyler and Howard (1969) give a value similar to the above for the refractivity of CO_2 under Martian conditions. A value of 2.44×10^{-18} for the molecular refractivity of Ne was derived from the refractive indexes tabulated in *Astrophysical Quantities* (1963). After specifying the fractional concentration f of each of these three atmospheric constituents at each level, the distribution of total number density N in the Martian atmosphere can be obtained from relationships such as

$$N_i = R_i/(n_{CO_2} f_{CO_{2_i}} + n_{N_2} f_{N_{2_i}} + n_{Ne} f_{Ne_i}) . \tag{13}$$

From the vertical distribution of total number density, the thermal structure of the Martian atmosphere can be obtained by integration of the hydrostatic law. The atmospheric temperature distribution in terms of the distribution of N is given by

$$T(h) = T(h_0)\frac{N(h_0)}{N(h)} + \frac{1}{kN(h)}\int_h^{h_0} g(\xi)\bar{m}(\xi)N(\xi)\, d\xi , \tag{14}$$

where h_0 is the level selected as the upper boundary of the lower atmosphere, k is Boltzmann's constant, g is the acceleration due to gravity, and $\bar{m}$ is the mean molecular mass. The level h_0 is chosen to correspond to the position of the zero-refractivity ledge (discussed in the previous section).

In the case of a homogenous atmosphere, the denominator of the right-hand side of Equation 13 is a constant, and $\bar{m}$ is independent of altitude. Thus, Equation 14 simplifies to

$$T(h) = T(h_0)\frac{R(h_0)}{R(h)} + \frac{\bar{m}}{kR(h)}\int_h^{h_0} g(\xi)R(\xi)\,d\xi \,. \tag{15}$$

By using the trapezoidal rule to integrate the refractivities in Equation 15, we obtain (for $i > i_0$)

$$T_i = T_{i_0}\frac{R_{i_0}}{R_i} + \frac{\bar{m}}{2kR_i}\sum_{j=i_0}^{i-1}(g_jR_j + g_{j+1}R_{j+1})\Delta h_{j,j+1} \,, \tag{16}$$

where i and i_0 are the indexes corresponding to altitudes h and h_0, respectively, and $\Delta h_{j,j+1}$ is the height increment between levels j and $j + 1$.

The first term on the right-hand side of Equation 16 depends upon T_{i_0}, the arbitrarily chosen temperature at the upper boundary of the lower atmosphere. This choice of boundary temperature, therefore, will to some degree influence the derived profile at lower altitudes. Because of its inverse dependence on the refractivity, however, the magnitude of this term decreases quite rapidly as deeper atmospheric levels are considered. The relationship between the refractivity distribution and the distribution of free electrons in the upper atmosphere (the region above the zero-refractivity ledge) is given by

$$N_{e_i} = -\frac{R_i\nu^2}{40.3 \times 10^{12}} \quad (\mathrm{cm}^{-3}) \,, \tag{17}$$

where ν is the frequency of the telemetry signal (approximately 2.2×10^9 Hz).

ERROR ANALYSIS

Both systematic and random errors are involved in the derivation of the physical characteristics of the Martian atmosphere from the occultation data. Errors of the former type arise from oscillator drift and imperfect knowledge of the spacecraft trajectory. Errors of the latter kind result from the noise level of the input data.

Our analysis assumes that the systematic errors are manifest in the large departures of the Doppler residuals from zero during the preencounter and postencounter periods, when the atmosphere on Mars cannot be modifying the spacecraft telemetry signal. These systematic errors are assumed to be removed, or largely reduced, by (1) performing a polynomial regression analysis on the data over selected time periods in the preencounter and postencounter phases, (2) extrapolating the resulting least-squares-fitted bias curve into the encounter period, and (3) subtracting this curve from the complete set of Doppler residuals to obtain a complete set of corrected residuals.

Since the error involved in extrapolating the bias curve through the encounter period cannot be formally estimated, we have placed the additional constraint of a near-zero-refractivity ledge, discussed previously, on the data-reduction process. However, even this constraint does not guarantee that the extrapolation error is negligible; the authors have therefore analyzed a large number of cases resulting from different polynomial fits to the raw residuals to assess the validity of this correction procedure and to establish the range of the systematic errors that persist if the assumption of a low-refractivity region is correct.

The polynomial regression analysis described above yields the variance of the Doppler residuals to which the bias curve is fitted. This variance is a measure of the noise level, or random error, inherent in the input data. As mathematical operations are performed, this initial random error will propagate through the analysis to all derived quantities. In contrast to the situation with regard to the systematic error described above, a formal procedure is available for calculating the resultant errors in quantities derived from the Doppler residuals.

Our analysis of the formal errors accumulated during the derivation of the atmospheric characteristics is based on the following assumptions:

(1) Systematic errors are removed by the procedure described above; thus, errors in the derived quantities, reflecting only the random noise in the input data, can be treated separately.

(2) The errors in the derived quantities result only from errors in the Doppler residuals. The uncertainties in other factors entering into the analysis, such as the wavelength of the telemetry signal and the spacecraft position, either are negligible compared with the errors in the residuals or are systematic and hence removed in the data reduction.

(3) The errors in the Doppler residuals are uncorrelated and statistically independent.

In accordance with the notation of the previous section, if σ_j^δ denotes the variance in the Doppler residuals at the jth level, where the superscript δ refers to Doppler residuals, the variance in a quantity Q derived from the residuals at the nth level is

$$\sigma_n^Q = \sum_{j=1}^{n} \left(\frac{\partial Q_n}{\partial \delta_j} \right)^2 \sigma_j^\delta \ , \tag{18}$$

where Q_n is the value of Q at the nth level, assumed to be a function of the Doppler residuals at level n and at all higher altitudes (i.e., at all levels $j \leq n$).

For the purposes of the following discussion, it is convenient to define two matrices $\mathbf{M}$ and $\mathbf{S}$ by

$$\mathbf{M}_{ij}^{Q\delta} = \frac{\partial Q_i}{\partial \delta_j} \ , \quad \mathbf{S}_{ij}^{Q\delta} = \left(\frac{\partial Q_i}{\partial \delta_j} \right)^2 \ . \tag{19}$$

Thus, the ijth element of the matrix $\mathbf{M}^{Q\delta}$ is the derivative of Q at altitude i with respect to δ at altitude j, and the matrix $\mathbf{S}^{Q\delta}$ is obtained by squaring the individual elements of $\mathbf{M}^{Q\delta}$. Since all derived quantities are obtained by downward integration from the top of the atmosphere, their values at a given

altitude do not depend on the Doppler residuals at lower altitudes. All of the matrices used in this analysis (with the single exception noted below) are, therefore, either lower triangular or diagonal. The specific methods used in obtaining the random error in the various atmospheric quantities derived from the Doppler residuals are enumerated below.

Phase Change

In view of Equation 2, the matrix elements involved in the calculation of the errors in the phase change are

$$\mathbf{M}_{ij}^{\phi\delta} = \begin{cases} 0\,, & \text{if } i = 1 \text{ or } i < j \\ \tfrac{1}{2}\Delta t_{j,j+1}\,, & \text{if } i > 1 \text{ and } j = 1 \\ \tfrac{1}{2}(\Delta t_{j-1,j} + \Delta t_{j,j+1})\,, & \text{if } 1 < j < i \\ \tfrac{1}{2}\Delta t_{j-1,j}\,, & \text{if } j = i > 1 \end{cases} \tag{20}$$

The phase-change variance is

$$\sigma^{\phi} = \mathbf{S}^{\phi\delta}\,\sigma^{\delta}\,, \tag{21}$$

where σ^{ϕ} is the vector whose components are the phase-change variances at points j, $\mathbf{S}^{\phi\delta}$ is defined by Equation 19, and σ^{δ} is the (constant) vector of the residual variance.

Straight-Line Approximation to Phase Change

The variance in Φ is given by

$$\sigma^{\Phi} = \mathbf{S}^{\Phi\delta}\,\sigma^{\delta}\,, \tag{22}$$

where σ^{Φ} is the vector whose components are the variances of Φ at levels j. In view of Equation 6, the matrix $\mathbf{S}^{\Phi\delta}$ is easily computed using Equation 19 once $\mathbf{M}^{\Phi\delta}$ is found from the equation

$$\mathbf{M}_{ij}^{\Phi\delta} \equiv \frac{\partial\Phi_i}{\partial\delta_j} = \frac{\partial\Phi_i}{\partial\phi_k}\frac{\partial\phi_k}{\partial\delta_j} + \frac{\partial\Phi_i}{\partial\alpha_k}\frac{\partial\alpha_k}{\partial\delta_j} \tag{23}$$

or

$$\mathbf{M}^{\Phi\delta} = \mathbf{M}^{\Phi\phi}\mathbf{M}^{\phi\delta} + \mathbf{M}^{\Phi\alpha}\mathbf{M}^{\alpha\delta}\,. \tag{24}$$

The matrices $\mathbf{M}^{\Phi\phi}$ and $\mathbf{M}^{\Phi\alpha}$ are calculated directly from Equation 6 by using Equation 19, with ϕ and α replacing δ. We may note that $\mathbf{M}^{\Phi\phi} = \mathbf{U}$, the unit matrix, whereas $\mathbf{M}^{\Phi\alpha}$ is a constant multiple of the unit matrix. $\mathbf{M}^{\phi\delta}$ has already been computed in estimating the phase-change errors (Equation 20) and $\mathbf{M}^{\alpha\delta}$ is readily obtained from Equations 2 and 4. After carrying out the matrix multiplication in Equation 24, we obtain

$$\mathbf{M}_{ij}^{\Phi\delta} = \left[\frac{1}{2}\,\Delta t_{i-1,i}(1 - D_{1j}) - \frac{Z_{s_i}\alpha_i}{V_{s_i}}\right] D_{ij}\,, \tag{25}$$

where D_{ij} is the Kronecker delta.

Refractivity

The variance in refractivity is given by

$$\sigma^R = \mathbf{S}^{R\delta} \cdot \sigma^\delta \ . \tag{26}$$

The refractivities are not given explicitly as functions of the Doppler residuals but are expressed in Equation 12 as functions of the straight-line approximation to the phase change. The matrix $\mathbf{M}^{R\delta}$, required for the computation of $\mathbf{S}^{R\delta}$, may therefore be obtained from

$$\mathbf{M}^{R\delta} = \mathbf{M}^{R\Phi} \cdot \mathbf{M}^{\Phi\delta} \ , \tag{27}$$

where $\mathbf{M}^{R\Phi}$ is obtained from Equation 12, the recursion formulae for the refractivity at various atmospheric levels, and $\mathbf{M}^{\Phi\delta}$ has been calculated in Equation 25. If we define a matrix β as

$$\beta_{ii} = \frac{\lambda \cdot 10^6}{\Delta Z_{ii}}$$

and

$$\beta_{ij} = -2 \frac{\Delta Z_{ij}}{\Delta Z_{ii}} \ (i > j) \ , \tag{28}$$

the matrix $\mathbf{M}^{R\Phi}$ may be calculated from the equations

$$\mathbf{M}^{R\Phi}_{ii} = \beta_{ii} \tag{29}$$

and

$$\mathbf{M}^{R\Phi}_{ik} = \sum_{j=1}^{i-1} \beta_{ij} \mathbf{M}^{R\Phi}_{jk} \ (i > k) \ . \tag{30}$$

Electron Density

The basic equation for the variance in electron density is

$$\sigma^{Ne} = \mathbf{S}^{Ne\delta} \cdot \sigma^\delta \ . \tag{31}$$

The matrix $\mathbf{M}^{Ne\delta}$, required for the calculation of $\mathbf{S}^{Ne\delta}$, is obtained from

$$\mathbf{M}^{Ne\delta} = \mathbf{M}^{NeR} \cdot \mathbf{M}^{R\delta} \ , \tag{32}$$

where $\mathbf{M}^{NeR}$ is a multiple of the unit matrix computed directly from the relation in Equation 17 between electron density and refractivity and $\mathbf{M}^{R\delta}$ has been calculated in Equation 27. The matrix $\mathbf{M}^{NeR}$ is given by

$$\mathbf{M}^{NeR}_{ij} = -\frac{\nu^2}{40.3 \times 10^{12}} D_{ij} \ . \tag{33}$$

Temperature

The temperature variance is given by

$$\sigma^T = \mathbf{S}^{T\delta} \cdot \sigma^\delta \ . \tag{34}$$

The matrix $\mathbf{M}^{T\delta}$ is obtained from

$$\mathbf{M}^{T\delta} = \mathbf{M}^{TR} \cdot \mathbf{M}^{R\delta} \ , \tag{35}$$

where $\mathbf{M}^{R\delta}$ has been calculated in Equation 27 and $\mathbf{M}^{TR}$ may be computed from the expression (Equation 16) relating temperature to refractivity. Since the temperature at the top of the lower atmosphere T_{i_0} is computed from the scale height determined by the two uppermost refractivity points, the matrix $\mathbf{M}^{TR}$ has a single nonzero element above the diagonal. The matrix elements corresponding to derivatives of the temperature at the initial altitude are

$$\mathbf{M}_{11}^{TR} = \frac{\bar{m}\bar{g}}{k} \Delta h_{12} \frac{1}{R_1} \left(\ln \frac{R_2}{R_1} \right)^{-2} \tag{36}$$

and

$$\mathbf{M}_{12}^{TR} = -\frac{R_1}{R_2} \mathbf{M}_{11}^{TR} \ , \tag{37}$$

where $\bar{g}$ is the average value of the acceleration due to gravity in the uppermost layer Δh_{12}. If we use the trapezoidal rule to integrate the refractivities in Equation 16, the diagonal matrix elements of $\mathbf{M}^{TR}$ are

$$\mathbf{M}_{ii}^{TR} = -\frac{T(h_0)R(h_0)}{R_i^2} + \frac{\bar{m}}{kR_i} \left(\frac{g_i}{2} \Delta h_{i-1,i} - \frac{1}{R^2} \cdot \chi \right) \qquad (i > 1) \ , \tag{38}$$

where

$$\chi = (g_1 R_1 + g_2 R_2) \frac{\Delta h_{12}}{2} + \cdots + (g_{i-1} R_{i-1} + g_i R_i) \frac{\Delta h_{i-1,i}}{2} \ . \tag{39}$$

The off-diagonal elements are

$$\mathbf{M}_{ij}^{TR} = \frac{\bar{m}}{2kR_i} (g_{j-1} \Delta h_{j-1,j} + g_j \Delta h_{j,j+1}) \qquad (i > j) \ . \tag{40}$$

The standard deviation in a quantity at a given altitude is the square root of the variance at that altitude, and the 3σ errors quoted below are three times the various standard deviations so obtained.

RESULTS

The results presented here were obtained by processing the *averaged* sets of Doppler data at each of the four Mariner occultation points. In all four cases, analysis of the sets of data taken by the individual DSN stations produced results that are closely similar to those described here.

The profiles of phase change, refractivity, electron density, temperature, and pressure shown were derived by considering 300 different polynomial fits to the raw residual data at each of the Mariner 6 and 7 occultation points. All of these fits were consistent with the zero-refractivity-ledge assumption, described above; i.e., they led to refractivity levels in the middle atmosphere between -0.05 and $+0.05$ n-unit. The heavy curves in Figures 11 through 24 correspond to the averages of 300 profiles of the phase change and derived atmospheric parameters at each of the occultation points. The crosshatched areas surrounding the heavy curves in these figures correspond to the $\pm 3\sigma$ range in each parameter, obtained from the ensemble of the 300 cases. This range can be considered a measure of the systematic error produced by the imperfect removal of the nonatmospheric components in the raw residual data. The areas bracketing the zones of systematic error in these figures represent the uncertainty, in each parameter, due to the growth of formal errors in the calculations.

The coordinates, local time, and local zenith angle at the four occultation points are given in Table 1. The season on Mars at the time of the Mariner 6 and 7 encounters was early fall in the northern hemisphere, with a solar declination of about 8°S.

In Figures 11 through 14, the straight-line approximation to the phase change is shown as a function of distance from the limb of Mars along the perpendicular to the Earth-Mars line at the four occultation points. In all four cases, the actual phase change differs only slightly from the straight-line approximation shown throughout most of the encounter period; the maximum difference is about 30 percent at the surface, in the case of Mariner 6 exit. The systematic and formal errors in the actual phase change are also closely similar to those bracketing the curves shown. This is a result of the small bending angle produced by the thin Martian atmosphere. This angle reaches a maximum of about 0.35 mrad at the surface of Mars, in the case of Mariner 6 exit. No evidence of an ionospheric-induced phase change was found in the Mariner 6 and 7 exit cases, which occurred at nighttime on Mars; and in these cases, only the phase change due to the lower atmosphere is shown (Figures 12 and 14). The absence of a region of detectable negative refractivity at the exit points in the upper atmosphere of Mars results in a larger positive phase change as occultation is approached. The presence of a spherical shell of negative refractivity at high altitudes with the properties predicted for the Martian ionosphere (Stewart and Hogan, 1969) would contribute negatively by about 10 cycles to the phase change experienced by a ray passing near the surface in a one-way transit of the atmosphere.

Profiles of atmospheric refractivity at the four occultation points are shown in Figures 15 through 18. In each case, these curves are averages of the 300 refractivity profiles obtained by inversion of the 300 individual phase curves whose average properties are depicted in Figures 11 through 14. The error zones surrounding the refractivity profiles were obtained as discussed above.

Averages of 300 profiles of electron density in each of the Mariner 6 and 7 entry cases are presented in Figures 19 and 20, along with their accompanying systematic and formal ($\pm 3\sigma$) error limits. As can be seen, the uncertainty in electron density resulting from formal errors is larger by an order

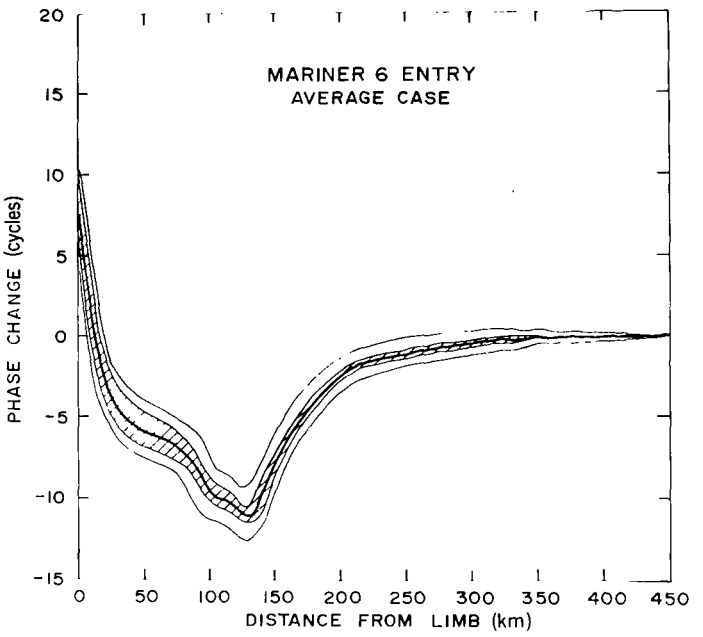

Figure 11—Phase change vs. distance from limb of Mars for Mariner 6 entry case. Error bars are $\pm 3\sigma$. (See text for explanation.)

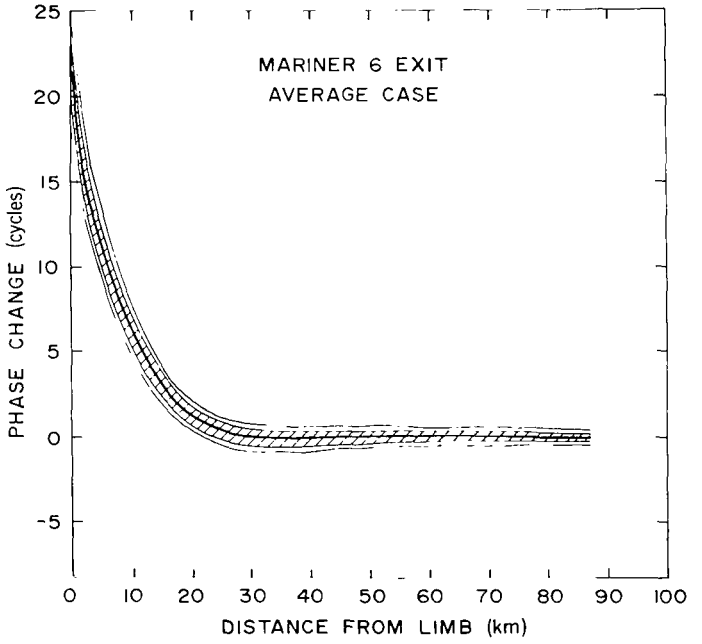

Figure 12—Phase change vs. distance from limb of Mars for Mariner 6 exit case. Error bars are $\pm 3\sigma$. (See text for explanation.)

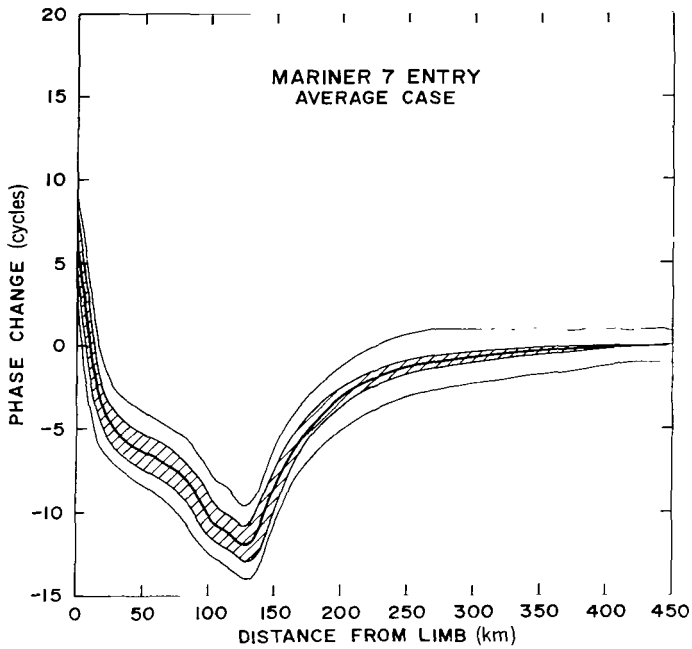

Figure 13—Phase change vs. distance from limb of Mars for Mariner 7 entry case. Error bars are $\pm 3\sigma$. (See text for explanation.)

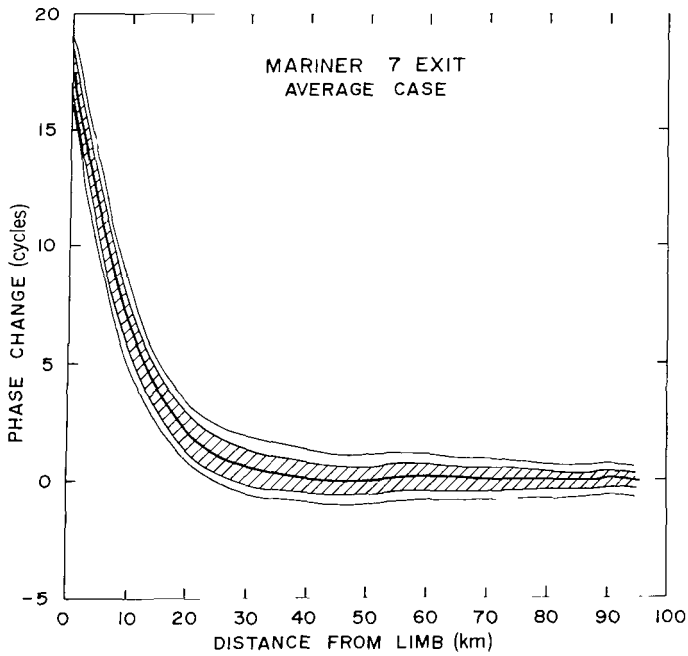

Figure 14—Phase change vs. distance from limb of Mars for Mariner 7 exit case. Error bars are $\pm 3\sigma$. (See text for explanation.)

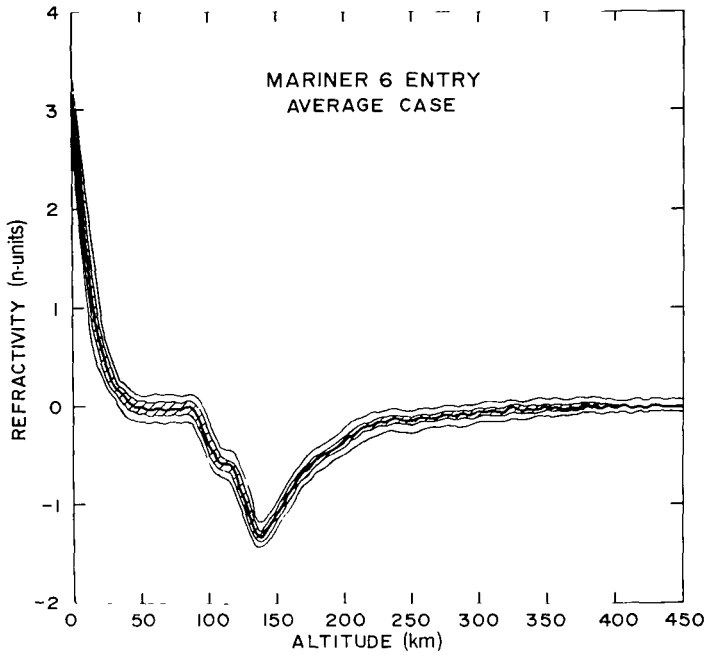

Figure 15—Refractivity vs. altitude for Mariner 6 entry. Error bars are $\pm 3\sigma$. (See text for explanation.)

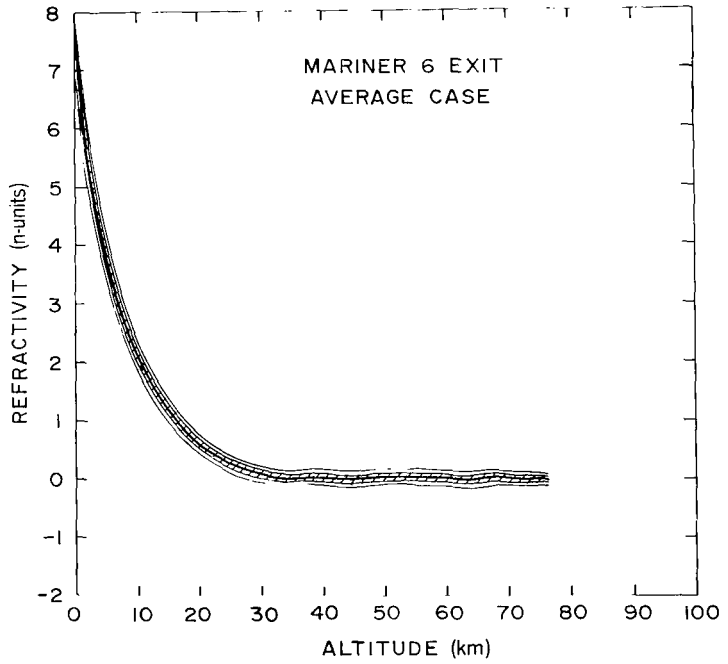

Figure 16—Refractivity vs. altitude for Mariner 6 exit. Error bars are $\pm 3\sigma$. (See text for explanation.)

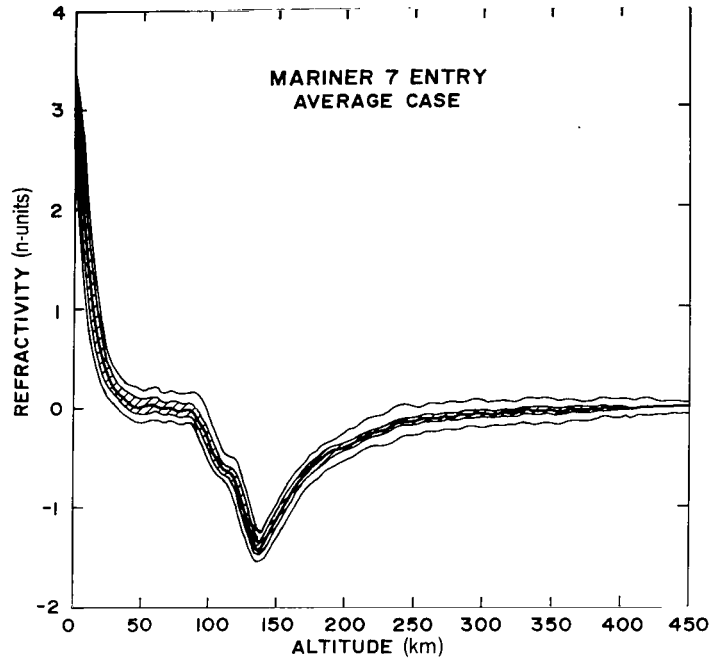

Figure 17—Refractivity vs. altitude for Mariner 7 entry. Error bars are $\pm 3\sigma$. (See text for explanation.)

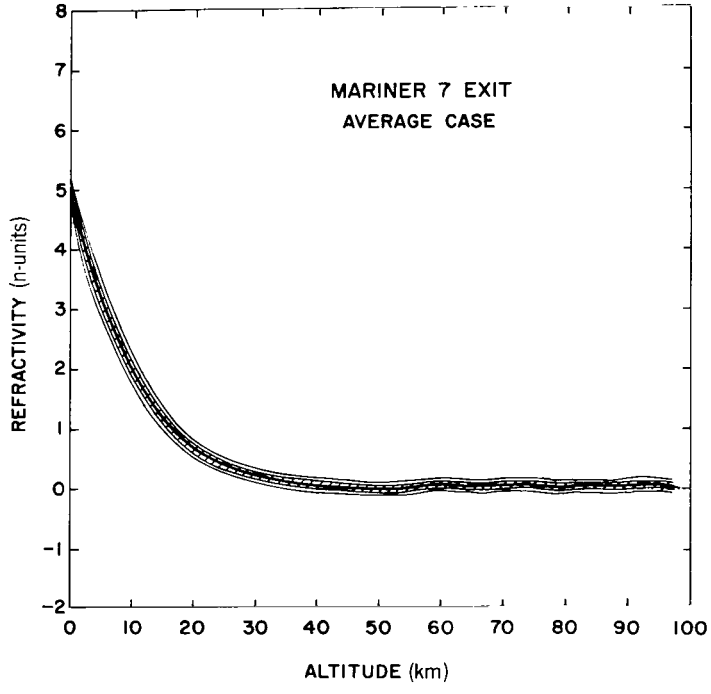

Figure 18—Refractivity vs. altitude for Mariner 7 exit. Error bars are $\pm 3\sigma$. (See text for explanation.)

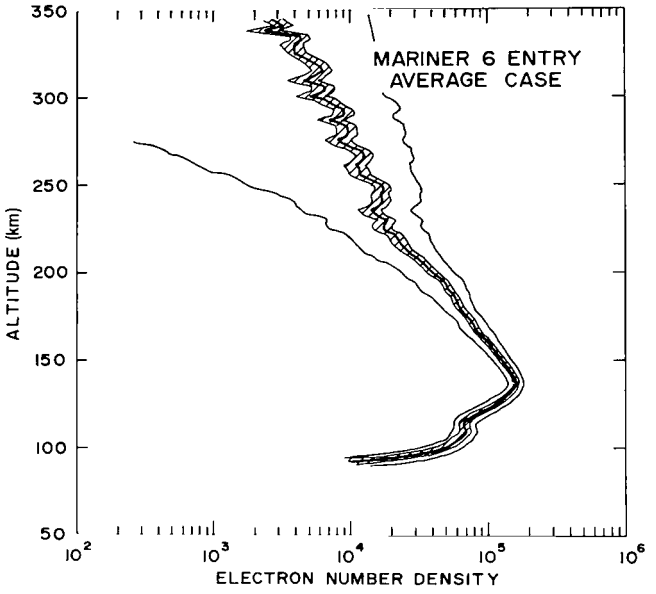

Figure 19—Electron number density (cm^{-3}) vs. altitude for Mariner 6 entry. Error bars are $\pm 3\sigma$. (See text for explanation.)

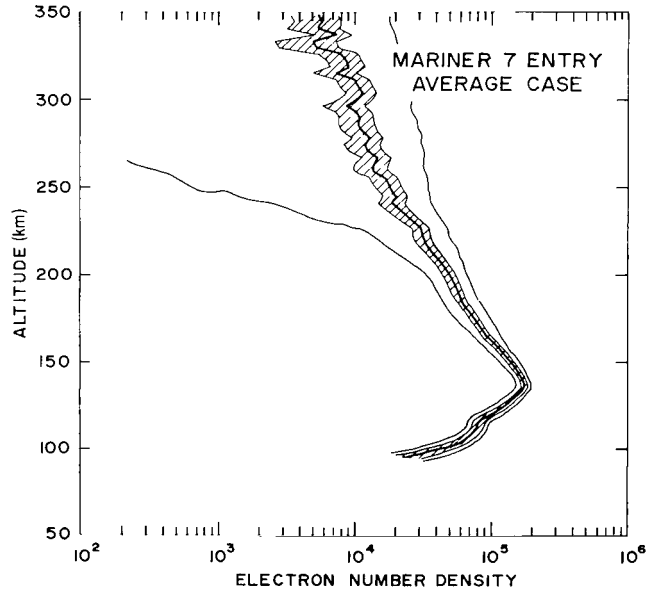

Figure 20—Electron number density (cm^{-3}) vs. altitude for Mariner 7 entry. Error bars are $\pm 3\sigma$. (See text for explanation.)

Table 1—Occultation parameters.

Occultation	Latitude	Longitude	Local Time	Local Solar Zenith Angle (deg)
Mariner 6 entry	3.7°N	355.7°E	1545	57
Mariner 6 exit	79.3°N	87.1°E	2210	107
Mariner 7 entry	58.2°N	30.3°E	1430	56
Mariner 7 exit	38.1°N	211.7°E	0310	130

of magnitude than that resulting from systematic errors. For the Mariner 6 and 7 entry cases, the average peak electron densities are 1.59 cm^{-3} at 136.5 km and 1.73 cm^{-3} at 137.5 km, respectively. The formal error limits ($\pm 3\sigma$) on the electron density at the peak are about $\pm 2.0 \times 10^4$ cm^{-3} in both cases. Determinations of the scale height of ionization between 150 and 225 km in these cases were made by fitting a straight line to the logarithms of the electron densities at intermediate levels. For the average of 300 cases, the topside scale heights are 43.0 km and 47.0 km, respectively, with formal ($\pm 3\sigma$) uncertainties of ±6.0 km and ±4.0 km. With the assumption of a 100 percent CO_2 atmosphere at these levels, the corresponding topside temperatures are 388 ± 54 K in the case of Mariner 6 entry, and 424 ± 35 K in the case of Mariner 7 entry, where the error bars on temperature correspond to the formal ($\pm 3\sigma$) errors. The larger error limits on the topside temperature in the Mariner 6 entry case are due to the presence of a dip in the electron profile above about 200 km (Figure 19).

In Figures 21 through 24, the averages of 300 temperature profiles and the attendant errors are shown for each of the four occultation points, for an assumed atmospheric composition of 100 percent CO_2. In these figures, the profile of the saturation temperature of CO_2 is shown as circles. In Table 2, the values of atmospheric temperature and pressure at the surface of Mars, with the estimated uncertainties due to both systematic and formal errors, are given for the four occultation points. Ionospheric parameters are also indicated in this table.

The effect of the adopted values of the occultation times on the derived values of the atmospheric parameters at the surface was estimated by varying this quantity by ±0.1 s. In all cases, the temperature at the surface varied by less than ±2 K, and the pressure at the surface varied by less than ±0.5 mb.

Temperature distributions were also derived for 95 percent CO_2, 5 percent N_2 and 90 percent CO_2, 10 percent Ne mixtures. The results of these calculations, also averaged over 300 cases, are shown in Figures 25 through 28, along with the average profiles obtained for the 100 percent CO_2 cases. In deriving these profiles, the temperature was constrained by the saturation temperature of CO_2. Since the observed refractivity scale height essentially fixes the ratio of temperature to mean molecular mass, the effect of the presence of lighter gases such as N_2 or Ne in the atmosphere is to lower the temperature while increasing the pressure. For clarity, the error zones have been omitted from these figures. The errors are of magnitude similar to the corresponding cases shown in Figures 21 through 24.

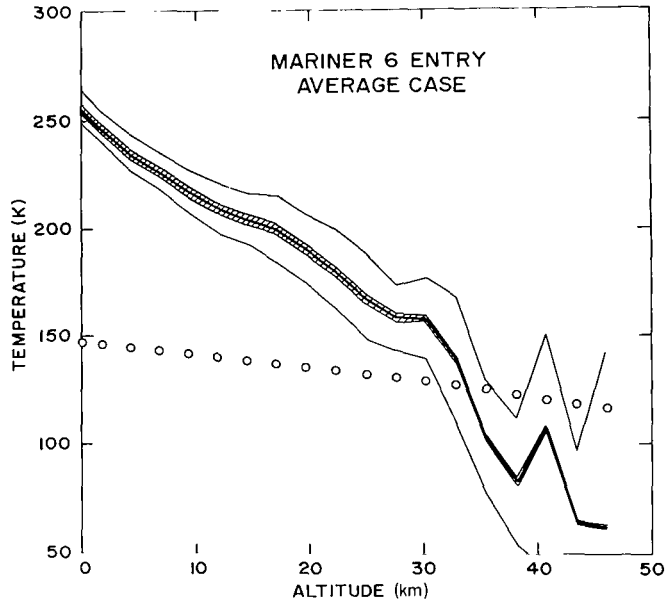

Figure 21—Temperature vs. altitude at Mariner 6 entry. Saturation temperature of CO_2 is shown as circles. Systematic error bars are $\pm 3\sigma$; formal error bars are $\pm\sigma$. (See text for explanation.)

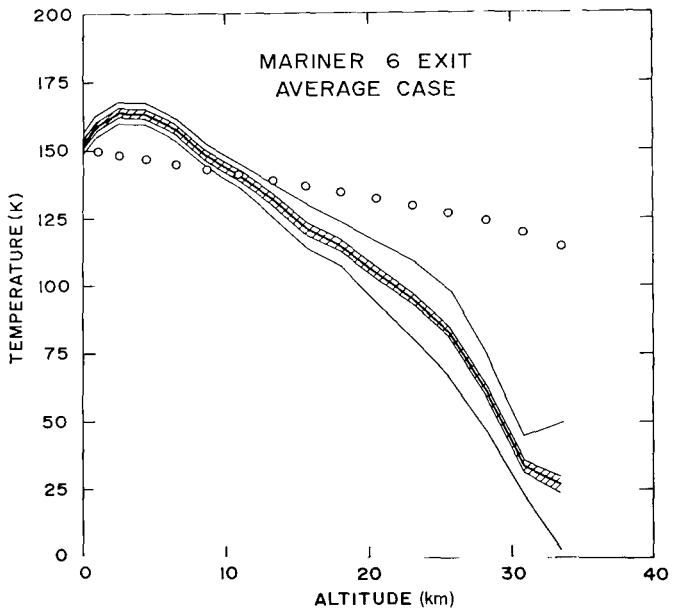

Figure 22—Temperature vs. altitude at Mariner 6 exit. Saturation temperature of CO_2 is shown as circles. Systematic error bars are $\pm 3\sigma$; formal error bars are $\pm\sigma$. (See text for explanation.)

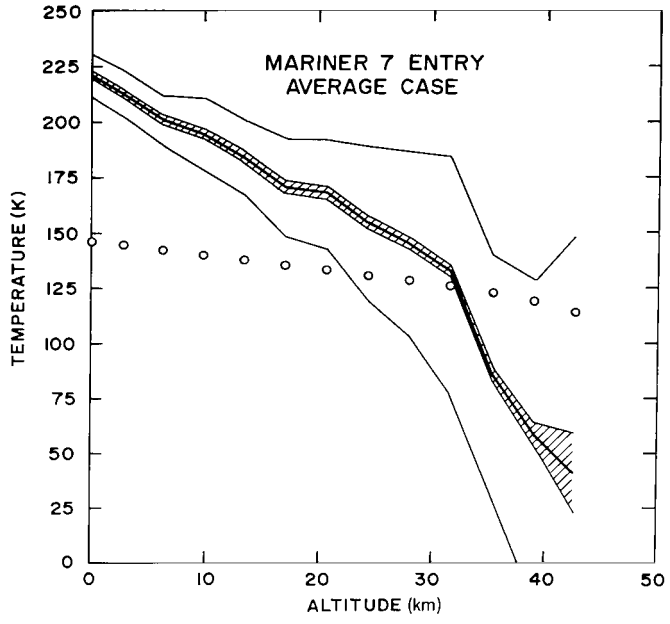

Figure 23—Temperature vs. altitude at Mariner 7 entry. Saturation temperature of CO_2 is shown as circles. Systematic error bars are $\pm 3\sigma$; formal error bars are $\pm\sigma$. (See text for explanation.)

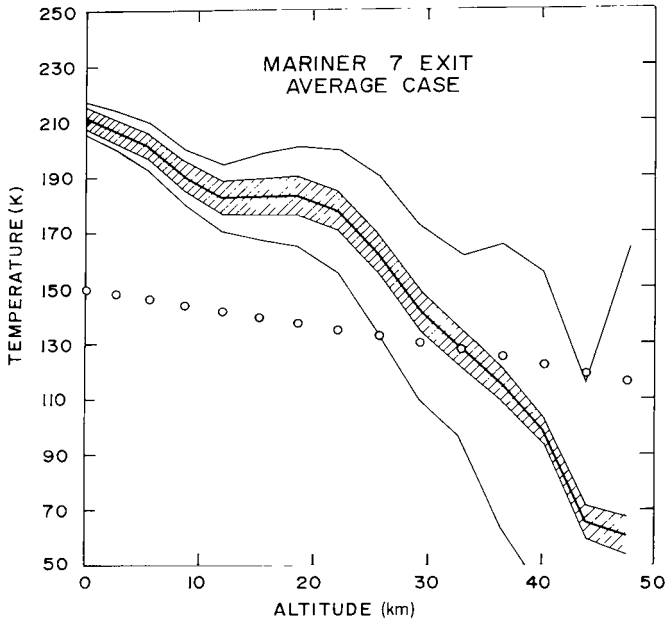

Figure 24—Temperature vs. altitude at Mariner 7 exit. Saturation temperature of CO_2 is shown as circles. Systematic error bars are $\pm 3\sigma$; formal error bars are $\pm\sigma$. (See text for explanation.)

Table 2—Atmospheric parameters on Mars from Mariners 6 and 7.

Event	Surface Temperature* (K)	Surface Pressure* (mb)	Maximum Electrons** ($\times 10^5$ cm^{-3})	Peak Altitude (km)	Topside Scale Height** (km)	Topside Temperature** (K)
Mariner 6 entry	254 ± 7	6.07 ± 0.36	1.59 ± 0.2	136.5	43± 6	388 ± 54
Mariner 6 exit	152 ± 5	8.51 ± 0.48	—	—	—	—
Mariner 7 entry	221 ± 8	4.95 ± 0.24	1.73 ± 0.2	137.5	47 ± 4	424 ± 35
Mariner 7 exit	209 ± 6	8.02 ± 0.45	—	—	—	—

*100 percent CO_2 atmosphere. Error bars correspond to $\pm\sigma$ formal errors plus $\pm 3\sigma$ systematic errors.
**Error bars correspond to $\pm 3\sigma$ formal errors plus $\pm 3\sigma$ systematic errors.

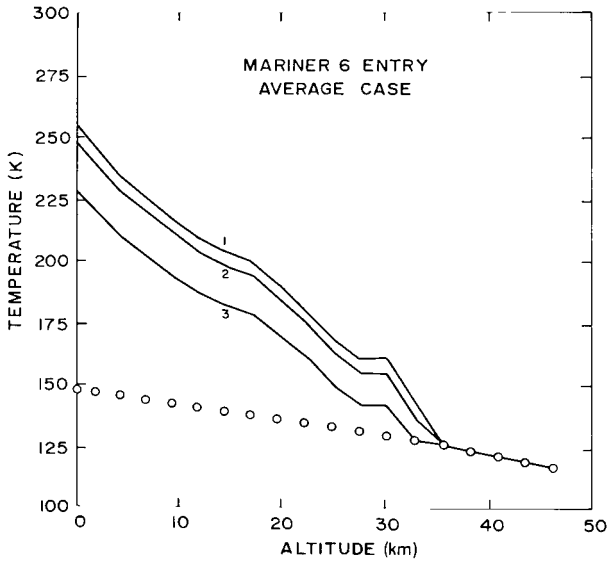

Figure 25—Temperature vs. altitude for Mariner 6 entry. Saturation temperature of CO_2 is shown as circles. Curve 1—100 percent CO_2; Curve 2—95 percent CO_2, 5 percent N_2; Curve 3—90 percent CO_2, 10 percent Ne.

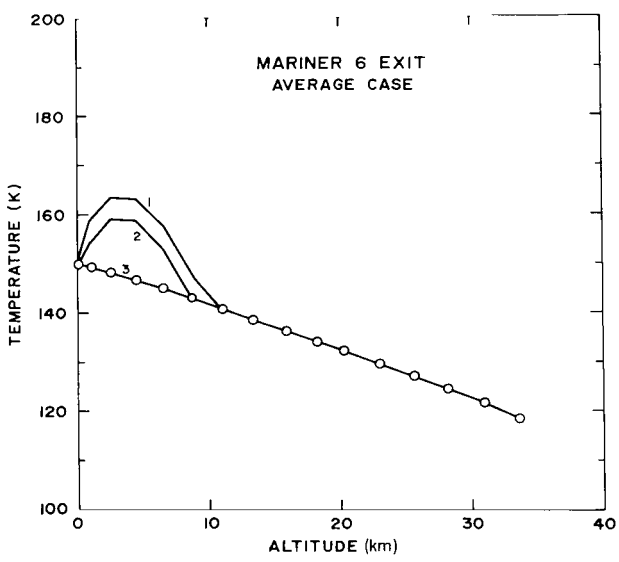

Figure 26—Temperature vs. altitude for Mariner 6 exit. Saturation temperature of CO_2 is shown as circles. Curve 1—100 percent CO_2; Curve 2—95 percent CO_2, 5 percent N_2; Curve 3—90 percent CO_2, 10 percent Ne.

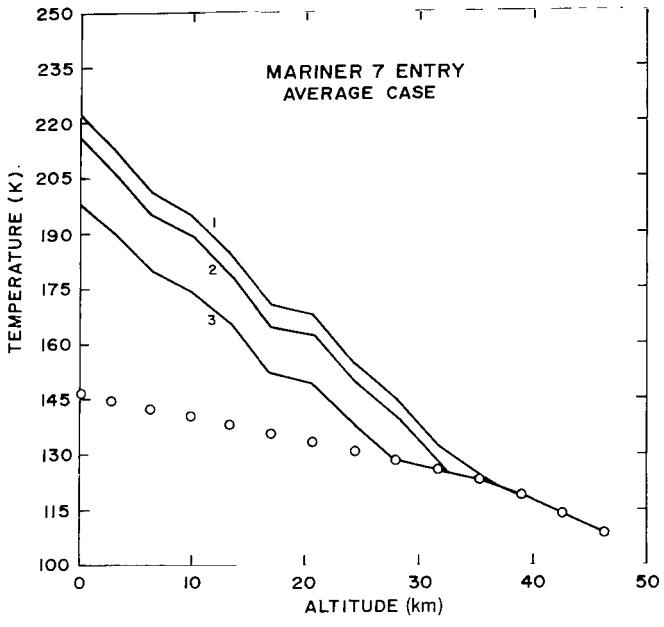

Figure 27—Temperature vs. altitude for Mariner 7 entry. Saturation temperature of CO_2 is shown as circles. Curve 1—100 percent CO_2; Curve 2—95 percent CO_2, 5 percent N_2; Curve 3—90 percent CO_2, 10 percent Ne.

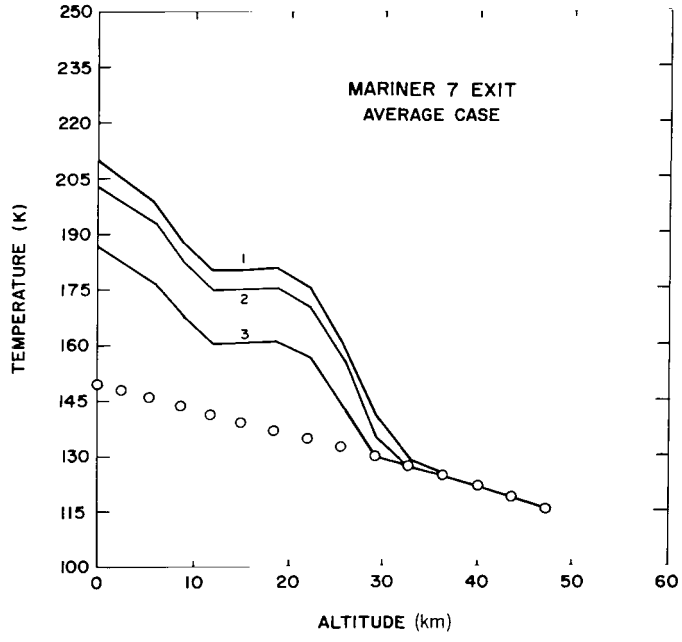

Figure 28—Temperature vs. altitude for Mariner 7 exit. Saturation temperature of CO_2 is shown as circles. Curve 1—100 percent CO_2; Curve 2—95 percent CO_2, 5 percent N_2; Curve 3—90 percent CO_2, 10 percent Ne.

The pressure distributions at the four occultation points (averages of 300 cases) for an atmosphere of 100 percent CO_2 are shown in Figure 29.

DISCUSSION

The Mariner 6 and 7 temperature profiles shown in Figures 21 through 24 are similar to those published by Rasool et al. (1970). The principal difference is in the Mariner 6 exit profile, which is now about 10 K colder at all altitudes than the corresponding profile obtained in the earlier analysis. As noted above, the results of Rasool et al. were based on a single reduction of the residual data and employed a different bias-removal technique. Since the present results are based on more extensive analyses of the data, they should be regarded as more reliable.

The temperature profiles of Figures 21 through 24 contain several features of interest. In all of the thermal profiles derived from the Mariner 6 and 7 occultation experiments, temperatures in the middle atmosphere fall below the value at which CO_2 would saturate. This drop in temperature is sharp; in all four cases, lapse rates in excess of adiabatic are found throughout an atmospheric layer several kilometers thick. In some cases, lapse rates as high as 10 K/km are obtained.

The indication of CO_2 saturation in the middle atmosphere is the most pervasive single feature of the derived temperature profiles; it occurs regardless of the details of the raw data adjustment. If the occultation data alone suggested CO_2 saturation in the middle atmosphere, this result would have to be viewed with some skepticism; the relative errors in refractivity are largest in this region where refractivities are small and the corresponding errors in the derived temperatures are large (Figures 21 through 24). The fact that all of the temperature profiles show this effect would imply that it is real, although an alternate explanation, in terms of the possible existence of a Martian D-region ionosphere, was pointed out by Rasool et al. (1970). There are other indications, however, apart from the occultation data, which suggest that CO_2 condensation does occur in the middle atmosphere.

The infrared spectrometers aboard both Mariners 6 and 7 recorded a reflection at 4.3 μm from altitudes well above the planetary surface (Herr and Pimentel, 1970). At the second Mariner 7 bright-limb crossing, the experimenters estimate the altitude of the reflecting feature to be 25 ± 7 km. This reflection spike indicates the presence of condensed CO_2 in the Mars middle atmosphere.

A third line of evidence suggesting possible CO_2 condensation comes from the Mariner 6 and 7 TV pictures (Leovy et al., 1971), where thin haze layers at altitudes ranging from 5 to 50 km above the limb of Mars were observed in several frames. Some of these layers are high enough in the atmosphere so that the scattering could be due to solid CO_2, although, as noted by Leovy et al. (1971), the lower layers seem to require another mechanism.

As pointed out above, prior to the Mariner 6 and 7 experiments, no theoretical models of the Martian lower atmosphere predicted condensation of CO_2. However, Gierasch (1971) has recently suggested that the kinetic energy generated by buoyancy might not be dissipated locally on Mars; this would result in the penetration of turbulent motions into what would otherwise be a stable radiative regime. Such overshooting would raise the tropopause level, producing substantially lower temperatures in the middle atmosphere. According to Gierasch (1971), at low latitudes the temperature would be driven low enough by this process for CO_2 to condense. The present results indicate, however, that

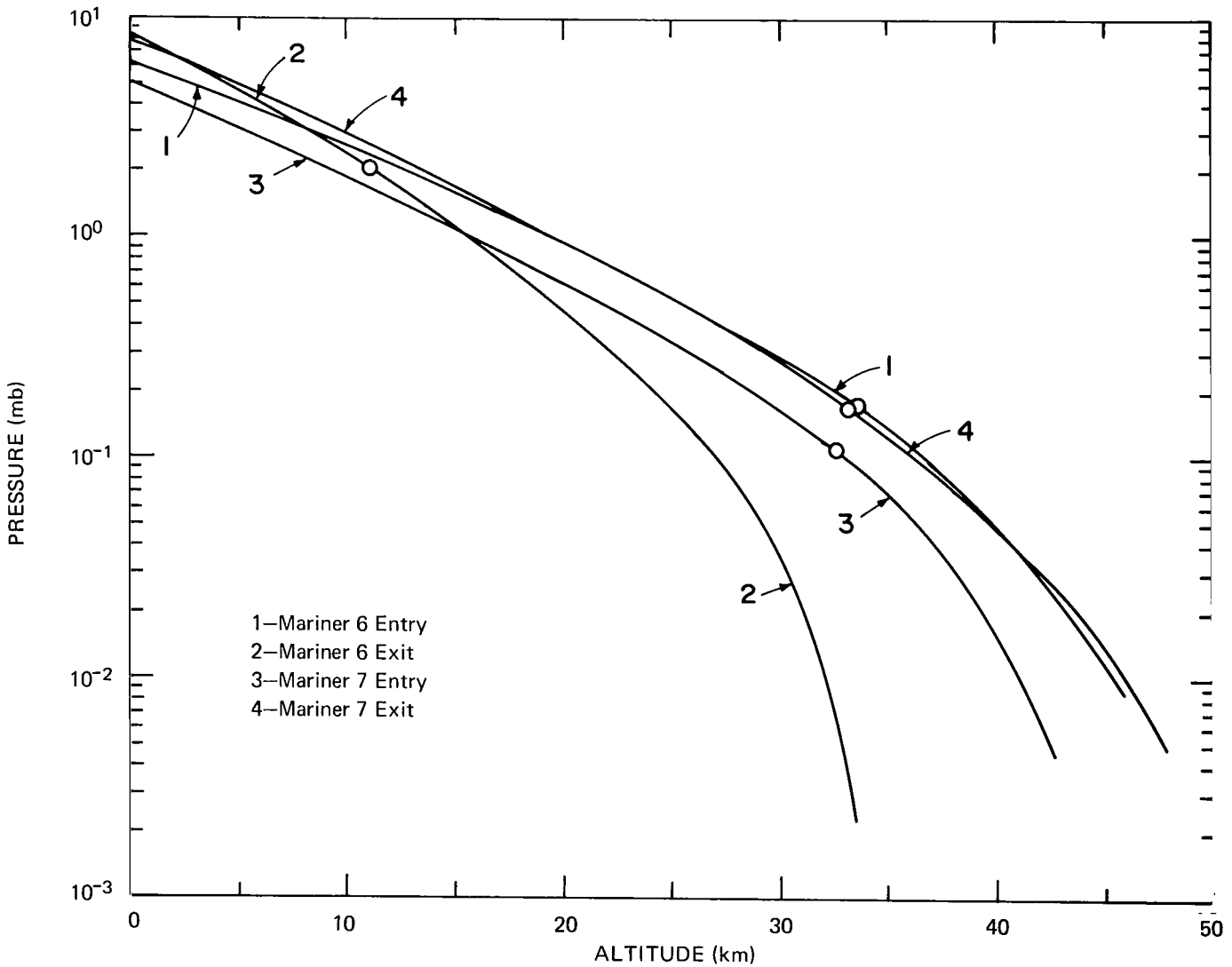

Figure 29—Pressure vs. altitude at the four occultation points for an atmosphere of 100 percent CO_2. Range in observed surface-pressure levels corresponds to about a 4-km altitude range, based on a pressure scale height of 10 km.

condensation occurs at high as well as low latitudes, and that the temperature gradient in the lowest 20 km of the atmosphere is subadiabatic. Neither of these findings is consistent with the theory of Gierasch, and it appears that at present there is no complete explanation for the thermal structures indicated in Figures 21 through 24.

The temperature obtained here for the atmosphere near the surface at the Mariner 6 entry point is 254 ± 7 K, whereas the *ground* temperature obtained with the infrared radiometer for the same region is 275 ± 5 K (Neugebauer et al., 1969 and 1971). Thus, an air-ground temperature discontinuity of about 20 K in the late Martian afternoon is indicated. The existence of a sizable temperature discontinuity between the atmosphere and surface of Mars in the afternoon was predicted by Gierasch and Goody (1968). According to these authors, turbulent transfer is the dominant process for heat exchange in the lower atmosphere. For the estimates of the turbulent heat flux which they used, Gierasch and Goody obtained a maximum temperature discontinuity (ground minus air) of +65 K for early afternoon and −40 K for early morning hours. The present results are in agreement with the prediction that a sizable temperature discontinuity can exist at times at the surface of Mars. However, the observed discontinuity of +20 K, in contrast with the discontinuity of +40 K predicted for 1600 local time, indicates that the magnitude of turbulent heat transfer in the Martian boundary layer is probably higher than Gierasch and Goody assumed.

In the same context, the Mariner 6 exit profile, corresponding to 2200 local time, exhibits a strong inversion near the ground (Figure 22), with the maximum temperature occurring near 4 km, about 15 K higher than the temperature at the surface. A similar feature was obtained by Rasool et al. (1970) but was not present in the profiles of Kliore et al. (1970). On the other hand, the nightside profile at Mariner 7 exit does not exhibit an inversion (Figure 24), and, according to the time-dependent calculations of Gierasch and Goody (1968), all of the nightside profiles should be characterized by such a feature. However, the absence of an inversion in the Mariner 7 exit profile cannot be interpreted with certainty as a disagreement with theory, since the error bars derived for this case permit a mild inversion.

The observed differences in total pressure at various points on Mars (Table 2) are almost certainly due to the topography of the surface; the lower pressure values correspond to elevated regions, whereas the higher pressures indicate depressed areas. Because the pressure scale height in the lower atmosphere of Mars is about 10 km, the observed pressure extremes would correspond to altitude variations on the surface of as much as 4 km. These variations are consistent with the recent radar results of Pettengill et al. (1969) and with the variation in CO_2 abundance over the disk of Mars observed both in ground-based measurements (Belton and Hunten, 1971) and in the Mariner 6 and 7 data (Herr et al., 1970).

The basic results of the Mariner 6 and 7 occultation experiments for the upper atmosphere of Mars are the profiles of the distributions of electron density with altitude (Figures 19 and 20). Several points about these ionospheric profiles should be noted. The maximum electron density observed at the time of the Mariner 4 flight (near solar minimum) was $(9.0 \pm 1.0) \times 10^4$ cm^{-3}; this was found near 120 km (Fjeldbo and Eshleman, 1968). Four years later, during a period of intermediate solar activity, Mariners 6 and 7 observed electron densities between $(1.6 \pm 0.2) \times 10^5$ cm^{-3} and $(1.7 \pm 0.2) \times 10^5$ cm^{-3} near 135 km, an increase in ionization by nearly a factor of 2. Similar values were derived by Fjeldbo et al. (1970) for Mariners 6 and 7.

A factor to be noted here is the departure of the Martian ionosphere from spherical symmetry. Such a departure would be most important in the interpretation of the Mariner 6 data because the occulting ray in this case passed across the occultation point in the general direction of the subsolar point. As the subsolar point is approached, the locus of the maximum electron density decreases in altitude, whereas the magnitude of the local maximum increases. The total number of electrons along the ray path would thus be greater for rays passing below the maximum electron density at the occultation point. Thus, the altitude of the peak ionization obtained by assuming spherical symmetry in the inversion of the refractivity data would be below the actual altitude of peak ionization at the occultation point. On the basis of numerical experiments in which Chapman-type ionospheres with different peak electron densities, scale heights, and peak altitudes were fitted to the phase change data, the authors estimate that the error in the observed altitude of maximum ionization due to this effect would be between 1 and 3 km.

The primary electron-density maxima observed in the Mars upper atmosphere are now generally accepted to be F_1 ionospheric layers, although there is still some controversy as to whether they are in strict photochemical equilibrium (R. W. Stewart, 1971) or are modified via interaction with the solar wind (Cloutier et al., 1969). If the ultraviolet fluxes reported by Hall and Hinteregger (1970) are assumed to be the only source of ionization, the observed electron-density profiles exhibit excess ionization by as much as a factor of 2 over theoretical models (R. W. Stewart, 1971; Donahue, 1971).

If the major electron-density maximum in the Mars ionosphere is interpreted as an F_1-layer in photochemical equilibrium, the plasma scale heights above the peak can be used to infer an exospheric temperature. At the time of the Mariner 4 flight, the exospheric temperature obtained in this way was about 275 K (Fjeldbo and Eshleman, 1968). The Mariner 6 and 7 plasma scale heights of 43 km and 47 km, measured between altitudes of about 150 and 225 km at a time of increased solar activity, yield exospheric temperatures of 388 ± 54 K and 424 ± 35 K, respectively. Similar results were found by Fjeldbo et al. (1970). Also, there is an indication of a large increase in the plasma scale height above 225 km at both the Mariner 6 and 7 entry points. Such an increase was also found by Fjeldbo et al. (1970), who suggested that it might represent a change of the dominant ion species in an ionosphere in diffusive equilibrium. It may also be attributed to a transition from an ionospheric region in photochemical equilibrium to a region where ambipolar diffusion controls the distribution of ions.

Both these plasma scale heights (below 225 km) and the neutral scale heights of about 25 km deduced from the Mariner ultraviolet spectrometer data (A. I. Stewart, 1972) indicate substantially lower exospheric temperatures than were predicted on theoretical grounds by McElroy (1969) and Stewart and Hogan (1969). Also, the fact that the derived plasma scale height is approximately twice the neutral scale height observed implies the absence of any alteration of the plasma distribution by the solar wind.

In addition to the major ionization peak, all of the Mariner flights to Mars (and Venus) have observed a secondary electron ledge at lower altitudes (Figures 19 and 20). This ledge appears about 25 km below the primary maximum in the Mariner 6 and 7 cases and was observed in a similar position by Mariner 4. This secondary electron peak is analogous to the Earth's E-region. It appears naturally in theoretical models of the Mars and Venus ionospheres (e.g., R. W. Stewart, 1971) and is a consequence of ionization of atmospheric constituents by soft X-rays.

ACKNOWLEDGMENT

The authors wish to extend their thanks to Dr. A. Kliore for providing the Doppler residual and trajectory data and for several useful discussions regarding data-reduction procedures.

Goddard Space Flight Center
National Aeronautics and Space Administration
Greenbelt, Maryland, September 15, 1971
039-52-01-01-51

REFERENCES

Allen, C. W., ed., *Astrophysical Quantities,* Athlone Press, London, 1963, Second Ed.

Barth, C. A., Fastie, W. G., Hord, C. W., Pearce, J. B., Kelly, K. K., Stewart, A. I., Thomas, G. E., Anderson, G. P., and Raper, O. F., "Mariner 6: Ultraviolet Spectrum of Mars Upper Atmosphere", *Science* 165:1004, 1969.

Belton, M. J. S., and Hunten, D. M., "The Abundance and Temperature of CO_2 in the Martian Atmosphere", *Astrophys. J.* 145:454, 1966.

Belton, M. J. S., and Hunten, D. M., "The Distribution of CO_2 on Mars: A Spectroscopic Determination of Surface Topography", *Icarus*, 1971.

Cloutier, P. A., McElroy, M. B., and Michel, F. C., "Modification of the Martian Ionosphere by the Solar Wind", *J. Geophys. Res.* 74:6215, 1969.

Dalgarno, A., and McElroy, M. B., "Mars: Is Nitrogen Present?", *Science* 170:167, 1970.

Donahue, T. M., "Aeronomy of CO_2 Atmospheres: A Review", *J. Atmos. Sci.* 28:895, 1971.

Essen, L., and Froome, K. D., "The Refractive Indices and Dielectric Constants of Air and Its Principal Constituents at 24,000 Mc/s", *Proc. Phys. Soc. London, Sect. B* 64:862, 1951.

Fjeldbo, G., and Eshleman, V. R., "The Bistatic Radar-Occultation Method for the Study of Planetary Atmospheres", *J. Geophys. Res.* 70:3217, 1965.

Fjeldbo, G., and Eshleman, V. R., "The Atmosphere of Mars Analyzed by Integral Inversion of the Mariner 4 Occulation Data", *Planet. Space Sci.* 16:1035, 1968.

Fjeldbo, G., Kliore, A., and Seidel, B., "The Mariner 1969 Occultation Measurements of the Upper Atmosphere of Mars", *Radio Sci.* 5:381, 1970.

Gierasch, P. J., and Goody, R. M., "A Study of the Thermal and Dynamical Structure of the Martian Lower Atmosphere", *Planet. Space Sci.* 16:615, 1968.

Gierasch, P. J., "Dissipation in Atmospheres: The Thermal Structure of the Martian Lower Atmosphere With and Without Viscous Dissipation", *J. Atmos. Sci.* 28:315, 1970.

Hall, L. A., and Hinteregger, H. E., "Solar Radiation in the Extreme Ultraviolet and Its Variation With Solar Rotation", *J. Geophys. Res.* 75:6959, 1970.

Herr, K. C., Horn, D., McAfee, J. M., and Pimentel, G. C., "Martian Topography from the Mariner 6 and 7 Infra-Red Spectra", *Astron. J.* 75:883, 1970.

Herr, K. C., and Pimentel, G. C., "Evidence for Solid Carbon Dioxide in the Upper Atmosphere of Mars", *Science* 167:47, 1970.

Kliore, A. J., Cain, D. L., Levy, G. S., Eshleman, V. R., Fjeldbo, G., and Drake, F. D., "Occultation Experiment: Results of the First Measurement of Mars' Atmosphere and Ionosphere", *Science* 149:1243, 1965.

Kliore, A., Fjeldbo, G., Seidel, B. L., and Rasool, S. I., "Mariners 6 and 7: Radio Occultation Measurements of the Atmosphere of Mars", *Science* 166:1393, 1969.

Kliore, A., Fjeldbo, G., and Seidel, B. L., "Summary of Mariner 6 and 7 Radio Occultation Results on the Atmosphere of Mars", Paper No. m. 25, Open Meeting, Working Group 7, XIIIth Plenary Meeting of COSPAR, Leningrad, U.S.S.R., May 20-29, 1970.

Leovy, C. B., Smith, B. A., Young, A. T., and Leighton, R. B., "Mariner Mars 1969: Atmospheric Results", *J. Geophys. Res.* 76:297, 1971.

McElroy, M. B., "Structure of the Venus and Mars Atmospheres", *J. Geophys. Res.* 74:29, 1969.

Neugebauer, G., Munch, G., Chase, S. C., Jr., Hatzenbeler, H., Miner, E., and Schofield, D., "Mariner 1969: Preliminary Results of the Infrared Radiometer Experiment", *Science* 166:98, 1969.

Neugebauer, G., Munch, G., Kieffer, H., Chase, S. C., Jr., and Miner, E., "Mariner 1969 Infrared Radiometer Results: Temperatures and Thermal Properties of the Martian Surface", *Astron. J.* 76:719, 1971.

Owen, T., "The Composition and Surface Pressure of the Martian Atmosphere: Results From the 1965 Opposition", *Astrophys. J.* 146:257, 1966.

Pettengill, G. H., Counselman, C. C., Rainville, L. P., and Shapiro, I. I., "Radar Measurements of Martian Topography", *Astron. J.* 74:461, 1969.

Rasool, S. I., Hogan, J. S., Stewart, R. W., and Russell, L. H., "Temperature Distributions in the Lower Atmosphere of Mars From Mariner 6 and 7 Radio Occultation Data", *J. Atmos. Sci.* 27:841, 1970.

Spinrad, H., Schorn, R. A., Moore, R., Giver, L. P., and Smith, H. J., "High-Dispersion Spectroscopic Observations of Mars, 1, The CO_2 Content and Surface Pressure", *Astrophys. J.* 146:331, 1966.

Stewart, A. I., "Mariner 6 and 7 Ultraviolet Spectrometer Experiment: An Interpretation of the Intense CO_2^+, CO, and O Airglow Emissions", *J. Geophys. Res.* 77, 1972.

Stewart, R. W., and Hogan, J. S., "Solar Cycle Variation of Exospheric Temperatures on Mars and Venus: A Prediction for Mariners 6 and 7", *Science* 165:386, 1969.

Stewart, R. W., "The Electron Distributions in the Mars and Venus Upper Atmospheres", *J. Atmos. Sci.* 28, 1971.

Tyler, G. L., and Howard, H. T., "Refractivity of Carbon Dioxide Under Simulated Martian Conditions", *Radio Sci.* 4:899, 1969.

NASA-Langley, 1972 —— 30

"The aeronautical and space activities of the United States shall be conducted so as to contribute . . . to the expansion of human knowledge of phenomena in the atmosphere and space. The Administration shall provide for the widest practicable and appropriate dissemination of information concerning its activities and the results thereof."

— NATIONAL AERONAUTICS AND SPACE ACT OF 1958

NASA SCIENTIFIC AND TECHNICAL PUBLICATIONS

TECHNICAL REPORTS: Scientific and technical information considered important, complete, and a lasting contribution to existing knowledge.

TECHNICAL NOTES: Information less broad in scope but nevertheless of importance as a contribution to existing knowledge.

TECHNICAL MEMORANDUMS: Information receiving limited distribution because of preliminary data, security classification, or other reasons.

CONTRACTOR REPORTS: Scientific and technical information generated under a NASA contract or grant and considered an important contribution to existing knowledge.

TECHNICAL TRANSLATIONS: Information published in a foreign language considered to merit NASA distribution in English.

SPECIAL PUBLICATIONS: Information derived from or of value to NASA activities. Publications include conference proceedings, monographs, data compilations, handbooks, sourcebooks, and special bibliographies.

TECHNOLOGY UTILIZATION PUBLICATIONS: Information on technology used by NASA that may be of particular interest in commercial and other non-aerospace applications. Publications include Tech Briefs, Technology Utilization Reports and Technology Surveys.

Details on the availability of these publications may be obtained from:

SCIENTIFIC AND TECHNICAL INFORMATION OFFICE

NATIONAL AERONAUTICS AND SPACE ADMINISTRATION

Washington, D.C. 20546